A New Development of a Shadow Density Filter for Manufacturing Constraint and Its Applications to Multiphysics Topology Optimization

Gil Ho Yoon[1]
Professor
School of Mechanical Engineering,
Hanyang University,
Seoul 04763, Korea
e-mail: ghy@hanyang.ac.kr

Seon Il Ha
School of Mechanical Engineering,
Hanyang University,
Seoul 2220, Korea
e-mail: qwzxc12@gmail.com

The present research develops a new shadow filter and presents its usage for structural topology optimization (TO) considering the molding manufacturability. It is important to consider manufacturing methods in designing products. Some geometrical features not allowing molded parts should be removed. In addition, it has been an important issue to efficiently impose these manufacturing constraints in TO. For this purpose, the present research emulates implementation of shadowing of products and applies the shadow images as pseudo-density variables in TO. The use of this shadow density filter ensures that the optimized layouts comply with the conditions of the manufacturing constraints. Various manufacturing conditions can be imposed depending on the direction and the position of the light. Several numerical examples of compliance minimization problem, conjugate heat transfer problem, and fluid–structure interaction problem are solved to demonstrate the validity and effectiveness of the present shadow density filters, and their performances are compared. [DOI: 10.1115/1.4048818]

Keywords: topology optimization, manufacturing constraint, geometrical constraint, molding constraint, multiphsyics problem, design for manufacturing, design methodology, design optimization, multidisciplinary design and optimization

Introduction

This research presents a new *shadow* density filter in a topology optimization (TO) framework to effectively consider various geometric constraints of manufacturing methods with molds in metallurgy, casting, or injection processes (see Refs. [1–4] and the references therein). When engineers consider the molding process as a manufacturing technique for some components of their products, it is important that the shapes of the components allow the molded parts to be easily removed from the molds. Due to the difficulties in accurately predicting the metal/reign mold flow direction, it is hard to simultaneously consider the performances of the products and processability. Thus, the design for manufacturing (DFM) process should be adapted to consider the performance of products together with their manufacturing costs and manufacturability. DFM relies on qualified engineers and their experience [5–9]. From a structural topology optimization point of view, there are relevant researches considering the manufacturability [1–3,10–12]. In Ref. [1], the virtual scalar value problem is solved to enforce the manufacturing constraint. In Ref. [2], the pseudo light approach was proposed for the level-set approach. In Refs. [3,13], the design variables in two-dimensional domain are reduced to a vector to consider the manufacturing constraint. In Ref. [4], the manufacturing constraint is addressed and applied for aerospace component. To contribute this research topic without solving extra physics problem to impose the manufacturing constraint and maintaining the number of the design variables in topology optimization, this research develops a new concept called the shadow density filter for TO [1,2,14]. Compared with the relevant researches, the present shadow density filter does not solve the additional physics or reduce the number of the design variables.

Structural optimization has been widely used in engineering and sciences as a powerful tool in finding optimal structures based on mathematical optimization theory. Several types of structural optimizations exist including size, shape and topology. TO allows us to find new and sometimes unanticipated optimal topologies without a prior given topology, and it has been widely applied for complex multiphysics problems (see Refs. [15–18] and reference therein). Currently, many commercial software packages provide some functionalities of TO, and some successful industrial applications can be found. The solid isotropic material with penalization (SIMP) method is popular, and there are other parameterization approaches in topology optimization such as the level-set based topology optimization, the moving morphable component (MMC) approach [19,20], the wavelet-based approach, and the element connectivity parameterization method [21,22]. There has been an increase in studies focusing on manufacturability in TO (see Refs. [1–4,13,14,23] and the references therein). The TO method mainly considers the performance as an objective with a few constraints, therefore, the optimized structures should be interpreted and modified by engineers considering the manufacturing constraints they adopt. In other words, a topologically optimized design can be too complex to be manufactured, and some modifications to accommodate the manufacturing process are essential. However, these modifications can degrade the performance significantly, and some reckless modifications can ruin the important features of the optimized designs. Therefore, a fundamental question arises for the optimality of the modified design. To overcome this issue, manufacturing constraints have been introduced during optimization processes. As there are many kinds of manufacturing processes and conditions, it is very challenging to mathematically construct these conditions and processes and embed them in the framework of an optimization process.

[1]Corresponding author.

Contributed by the Design Automation Committee of ASME for publication in the Journal of Mechanical Design. Manuscript received July 4, 2019; final manuscript received September 24, 2020; published online November 20, 2020. Assoc. Editor: James K. Guest.

There have been some relevant studies to impose manufacturability in TO. First of all, the checkerboard and the hinge pattern control are part of the earlier geometric constraint (see Ref. [24] and the references therein). The minimum or maximum length scale constraints are also geometric constraints [11,25]. Recently, the additive manufacturing (AM) process has attracted many attentions. Because of the development of 3D printing, it becomes important to satisfy the overhang conditions in AM [26–28]. There are some relevant studies in topology optimization for molding constraints. In Ref. [29], Xia et al. presented a method restricting the motion of a free boundary using a level-set approach. In Ref. [23], the casting and milling constraints are imposed by the projection based algorithm. In Ref. [30], the undercut and overhang angle control is introduced. In Ref. [31], the manufacturing constraint was considered in a level-set approach. In Ref. [32], the projection based approach was introduced in topology optimization. In Ref. [33], the deep drawing constraint was considered by introducing the mid-surface design, including cutouts. In Refs. [3,13], the design variables in two-dimensional domain are reduced to a vector to consider the manufacturing constraint. In Ref. [4], the manufacturing constraint is addressed and applied for aerospace component considering the manufacturability. Shape feature control was proposed in the level-set approach in Ref. [34]. In Ref. [13], the multiaxis machining restrictions are considered.

The new shadow density method presented in this research imposes a manufacturing constraint that can be incorporated with the TO process. Specifically, the design variables of TO are filtered to prevent some geometric features that would prohibit the use of the molding manufacturing process. The shadows of the design variables are generated using simple multiplication and subtraction of the design variables for virtual lights, and these shadows are used as the pseudo densities to determine the stiffness matrices of the finite element simulation and the sensitivity analysis. Some void regions in these shadow images are surrounded by solid regions and are shadowed with virtual light and rendered as virtual solid regions. The undercut geometries can be shadowed in the direction of the virtual light, and the pseudo densities do not contain the geometric features of the undercut geometries. Therefore, we found that the present shadow density filtering approach can be incorporated with TO.

This paper is organized as follows. Section 2 describes the basic equations for the structural optimization problems. The development of the present shadow filter formulation is described in Sec. 3. Section 4 presents several numerical examples to show the advantages and disadvantages of the present shadow density filter. Section 5 presents the conclusions and suggests future research topics.

Topology Optimization Formulations

Compliance Minimization Problem. To illustrate the validity of the shadow filter, this research considers TO minimizing compliance subject to mass constraints based on the SIMP interpolation function. It is common to use the finite element formulation to solve the equilibrium equation on the domain Ω as follows:

$$div\,\boldsymbol{\sigma}(\mathbf{u}) + \mathbf{b} = 0 \quad \text{in } \Omega \tag{1}$$

The Cauchy stress tensor, displacement field vector, and body force are denoted by $\boldsymbol{\sigma}$, $\mathbf{u}$, and $\mathbf{b}$, respectively. The Neumann and the Dirichlet boundary conditions on $\partial\Omega$ are described as follows:

$$\begin{aligned} \boldsymbol{\sigma}\cdot\mathbf{n} &= \mathbf{f} \quad \text{on } \partial\Omega_N \\ \mathbf{u} &= \mathbf{0} \quad \text{on } \partial\Omega_D \end{aligned} \tag{2}$$

$$\boldsymbol{\sigma} = \mathbf{C}\boldsymbol{\varepsilon} \tag{3}$$

where $\mathbf{f}$ denotes surface traction and $\mathbf{n}$ denotes the unit normal vector. After applying the finite element procedure, we obtain the solution of the continuum structure. The following optimization problem is set up and solved

$$\begin{aligned} &\underset{\boldsymbol{\gamma}}{\text{Min}}\; c = \mathbf{F}^{\mathrm{T}}\mathbf{U} \\ &\text{subject to } V(\tilde{\boldsymbol{\gamma}}) \le \bar{V} \\ &\mathbf{K}(\tilde{\boldsymbol{\gamma}})\mathbf{U} = \mathbf{F},\ \tilde{\boldsymbol{\gamma}} = \Phi(\boldsymbol{\gamma}) \\ &\Phi\text{: Shadow filter, } \boldsymbol{\gamma} = [\gamma_1, \gamma_2, \gamma_3 \ldots \gamma_{nel}] \end{aligned} \tag{4}$$

Here, the stiffness matrix, the displacement, and the force vectors are denoted by $\mathbf{K}$, $\mathbf{U}$, and $\mathbf{F}$, respectively. The filtered design variable with the shadow density filter Φ is $\tilde{\boldsymbol{\gamma}}$. The number of elements is denoted by *nel*. The volume and the upper volume are denoted by V and $\bar{V}$, respectively. Considering the linear strain, the equilibrium equation is constructed as follows:

$$\mathbf{K}(\tilde{\boldsymbol{\gamma}})\mathbf{U} = \mathbf{F}, \quad \mathbf{K}(\tilde{\boldsymbol{\gamma}}) = \sum_{e=1}^{nel} \mathbf{k}_e(\tilde{\gamma}_e) \tag{5}$$

With the gradient-based optimizer, the sensitivity values of the objective and the constraint with respect to the eth element should be computed as follows:

$$\frac{dc}{d\gamma_e} = \frac{dc}{d\tilde{\boldsymbol{\gamma}}}\frac{d\tilde{\boldsymbol{\gamma}}}{d\gamma_e} = \frac{dc}{d\tilde{\boldsymbol{\gamma}}}\frac{d\Phi(\boldsymbol{\gamma})}{d\gamma_e} \quad \text{with } \frac{dc}{d\tilde{\gamma}_e} = -\mathbf{u}_e^{\mathrm{T}}\frac{d\mathbf{k}_e}{d\tilde{\gamma}_e}\mathbf{u}_e \tag{6}$$

$$\frac{dV}{d\gamma_e} = \frac{dV}{d\tilde{\boldsymbol{\gamma}}}\frac{d\tilde{\boldsymbol{\gamma}}}{d\gamma_e} = \frac{dV}{d\tilde{\boldsymbol{\gamma}}}\frac{d\Phi(\boldsymbol{\gamma})}{d\gamma_e} \tag{7}$$

The above gradient information can be efficiently obtained with any differentiable density filter. The optimization problem is solved with a finite element strategy using a gradient-based optimizer with sensitivity analysis. For the topology optimization, it is essential to interpolate the material properties with respect to the continuous density variable in the SIMP method to avoid the discrete 0–1(void or solid) optimization problem. The material property in the linear elasticity equation is interpolated as follows:

$$\mathbf{C}(\tilde{\boldsymbol{\gamma}}) = \mathbf{C}_0\tilde{\boldsymbol{\gamma}}^n \tag{8}$$

where the nominal constitute matrix is $\mathbf{C}_0$, and the penalization factor is n. This research adopts 3 for this value. Although the above formulations are formulated for the compliance minimization problem, they are capable of applying to other problems.

Heat Dissipation Problem With Forced Convection. In addition to the compliance minimization problem, this study also considers the topology optimization for heat dissipation structure with forced convection. The multiphyiscs system with the Navier–Stokes equation and the heat transfer equation are formulated as follows:

$$\begin{aligned} &\rho(\mathbf{v}\cdot\nabla)\mathbf{v} = \nabla\cdot\mathbf{T}_f - \alpha\mathbf{v} \quad \text{and} \quad -\nabla\cdot\mathbf{v} = 0 \text{ in } \Omega, \\ &\mathbf{T}_f = -p\mathbf{I} + \mu(\nabla\mathbf{v} + \nabla\mathbf{v}^{\mathrm{T}}) \end{aligned} \tag{9}$$

$$\nabla\cdot(k\nabla T) = (\rho C_p\mathbf{v})\cdot\nabla T \quad \text{in } \Omega \tag{10}$$

where the fluid velocity field and pressure of incompressible flow are denoted by $\mathbf{v}$ and p, respectively. The analysis domain is denoted by Ω. In Eq. (9), there is a viscous force, $\alpha\mathbf{v}$. The dynamic viscosity and the fluid density are denoted by μ and ρ, respectively. The fluid symmetric stress $\mathbf{T}_f$, i.e., the stress in the deformed fluid configuration, is given as Eq. (9). The temperature is denoted by T. The thermal conductivity and the specific heat capacity are denoted by k and C_p, respectively. The heat dissipation with forced convection is formulated in (10). With the appropriate boundary condition, it is possible to consider the coupled system (see Ref. [15] for more details). For topology optimization, the material properties in Eqs. (9) and (10) are be interpolated with respect to design variables ($\boldsymbol{\gamma}$) as Table 1.

Table 1 Interpolated material properties of the heat dissipation structure

	Heat transfer equation			Fluid equation
	K	C_p	ρ	Friction coefficient (α)
Solid domain ($\gamma = 1$)	k_s	C_s	ρ_s	$\alpha_{\max}$ (the maximum friction coefficient)
Thermo/hydraulic domain ($\gamma = 0$)	k_f	$C_f(<<C_s)$	ρ_f	0

Without loss of generality, the SIMP approach is used to interpolate these variables as follows:

$$k(\boldsymbol{\gamma}) = (k_s - k_f)\boldsymbol{\gamma}^n + k_f \tag{11}$$

$$C_p(\boldsymbol{\gamma}) = (C_s - C_f)\boldsymbol{\gamma}^n + C_f \tag{12}$$

$$\rho(\boldsymbol{\gamma}) = (\rho_s - \rho_f)\boldsymbol{\gamma}^n + \rho_f \tag{13}$$

$$\alpha(\boldsymbol{\gamma}) = \alpha_{\max}\boldsymbol{\gamma}^n \tag{14}$$

where the penalization factor is n. Note that although the problem is one of multiphysics problems, the formulations in (6) and (7) are still applicable.

Fluid–Structure Interaction Problem With Monolithic Approach. In addition to the compliance minimization problem and the heat dissipation structure design, a mechanism design considering the fluid–structure interaction with the shadow filter is considered. To achieve the topology optimization with fluid–structure interaction, the monotonic approach in a unified analysis domain is used.

During an optimization process, the fluid and structural domains continuously change their shapes and topologies that cause the differentiability issue in topology optimization. To resolve these complications, the finite deformation tensor was introduced to formulate the coupled multiphysics equations. This deformation tensor can be used to correlate the differential operators and the integral operators of the two undeformed/deformed configurations as well as the quantities of the two configurations such as mass density, strain, and volume as shown in (15)–(18)

$$\mathbf{x} = \mathbf{X} + \mathbf{u},$$

$$\mathbf{F} = \frac{\partial \mathbf{x}}{\partial \mathbf{X}},\ \mathbf{x}\text{: the current coordinate},\ \mathbf{X}\text{: the undeformed coordinate} \tag{15}$$

Differential operators:

$$\nabla_{\mathbf{X}} = \mathbf{F}^{\mathrm{T}}\nabla_{\mathbf{x}},\ \nabla_{\mathbf{x}} = \mathbf{F}^{-\mathrm{T}}\nabla_{\mathbf{X}} \tag{16}$$

Integral operators:

$$\int_{{}^{t}\Omega} ()d\Omega = \int_{{}^{0}\Omega} ()\|\mathbf{F}\|d\Omega \tag{17}$$

$${}^{0}\Omega = {}_{ms}^{0}\Omega \cup {}_{mf}^{0}\Omega,\ {}^{t}\Omega = {}_{ms}^{t}\Omega \cup {}_{mf}^{t}\Omega \tag{18}$$

where the undeformed fluid domain (${}_{mf}^{0}\Omega$) and the undeformed solid (${}_{ms}^{0}\Omega$) domain are defined inside ${}^{0}\Omega$ and the deformed fluid domain (${}_{mf}^{t}\Omega$) and the deformed solid domain (${}_{ms}^{t}\Omega$) are defined inside ${}^{t}\Omega$. By using the above finite deformation tensor, the Navier–Stokes equation at the deformed domain ${}^{t}\Omega$ in the monolithic approach can be formulated in the undeformed domain ${}^{0}\Omega$ as follows:

$$-\int_{{}^{0}\Omega} \delta\mathbf{v}^{\mathrm{T}}\{\rho(\mathbf{v}\cdot\mathbf{F}^{-\mathrm{T}}\nabla_{\mathbf{X}}\mathbf{v})\}\|\mathbf{F}\|d\Omega = \int_{{}^{0}\Omega} \mathbf{F}^{-\mathrm{T}}\nabla_{\mathbf{X}}\delta\mathbf{v}^{\mathrm{T}}\mathbf{T}_f\|\mathbf{F}\|d\Omega + \int_{{}^{0}\Omega} \alpha\delta\mathbf{v}^{\mathrm{T}}\mathbf{v}\|\mathbf{F}\|d\Omega - \int_{{}^{0}\Gamma_{p^*}} p_{p^*}\mathbf{n}d\Gamma \tag{19}$$

$$-\int_{{}^{0}\Omega} \delta p^{\mathrm{T}}\{(\nabla_{\mathbf{x}}\cdot\mathbf{v})\}\|\mathbf{F}\|d\Omega = 0 \tag{20}$$

$$\mathbf{T}_f = -p\mathbf{I} + \mu(\nabla_x\mathbf{v} + \nabla_x\mathbf{v}^{\mathrm{T}}) \tag{21}$$

Because the derivations and manipulations of the Navier–Stokes equations are lengthy, the final form defined at the undeformed domain ${}^{0}\Omega$ is provided by following the notations in Refs. [17,35]. With the finite deformation tensor in (22), the linear elasticity equation of the deformed domain is transformed into one of the undeformed domain. As the external elastic energy due to the fluid stress at the coupling boundary being is dependent on structural displacements, the deformation tensor is also applied after using the divergence theory for the right side of Eq. (22)

$$\int_{{}^{0}\Omega} \delta\mathbf{S}^{\mathrm{T}}\cdot\mathbf{T}_s d\Omega = \int_{{}^{0}\Omega} \Psi\cdot\mathbf{F}^{-\mathrm{T}}\delta\mathbf{S}(\mathbf{u},\delta\mathbf{u})^{\mathrm{T}}\cdot p\|\mathbf{F}\|d\Omega + \int_{{}^{0}\Omega} \Psi\cdot\mathbf{F}^{-\mathrm{T}}\delta\mathbf{u}\cdot\nabla_{\mathbf{X}}p\|\mathbf{F}\|d\Omega \tag{22}$$

$$\Psi = \begin{cases} 1 & \text{for solid domain} \\ 0 & \text{for fluid domain} \end{cases} \tag{23}$$

$$\mathbf{S} = \frac{1}{2}(\nabla_{\mathbf{X}}^{\mathrm{T}}\mathbf{u} + \nabla_{\mathbf{X}}\mathbf{u}),\ \mathbf{T}_s = \mathbf{C}\mathbf{S} \tag{24}$$

$$\mathbf{S}(\mathbf{u},\delta\mathbf{u}) = \frac{1}{2}(\nabla_{\mathbf{x}}^{\mathrm{T}}\mathbf{u} + \nabla_{\mathbf{x}}\mathbf{u}),\ \nabla_{\mathbf{x}} = \mathbf{F}^{-\mathrm{T}}\nabla_{\mathbf{X}} \tag{25}$$

where the linear strain $\mathbf{S}$ and the associate stress $\mathbf{T}_s$ are defined as above. The linear constitutive matrix is denoted by $\mathbf{C}$. By solving the coupled Eqs. (19) and (20) for the fluid and (22) for the solid, the steady-state fluid–structure interaction system can be analyzed successfully. The mutual coupling analysis of fluid and structure can be accomplished by interpolating Young's modulus of elasticity, the filter Ψ for fluid pressure, and the inverse permeability coefficients in Table 2.

Young's modulus of the fluid (C_f) is set to a much smaller value than the value of C_s. The following interpolation functions are used

$$C(\boldsymbol{\gamma}) = \boldsymbol{\gamma}^n(C_s - C_f) + C_f \tag{26}$$

$$\Psi(\boldsymbol{\gamma}) = \boldsymbol{\gamma}^{n_{filter}} \tag{27}$$

$$\alpha(\boldsymbol{\gamma}) = \alpha_{\max}\boldsymbol{\gamma}^{n_{per}} \tag{28}$$

Table 2 Interpolated material properties of the present monolithic approach for the fluid–structure interaction problem

	Linear elasticity equation		Fluid equation
	Young's modulus (C)	Filter for fluid stress (Ψ)	Inverse permeability (α)
Solid	C_s	1	$\alpha >> 0$
Fluid	$C_f \ll C_s$	0	0

Note: C_s and C_f are Young's moduli of the solid and fluid, respectively.

The penalty factors of the fluid pressure filter and inverse permeability are denoted by n_{filter} and n_{per}, respectively. Note that although the problem is one of the multiphysics problems, the formulations in (6) and (7) are still applicable.

New Approach: Shadow Density and Cap Filters

Shadow Density Filter. We developed the shadow density filter to impose manufacturability in TO and improve performance. As discussed before, some approaches have been developed in Refs. [1–3] to consider the manufacturing constraint. In Ref. [1], the virtual scalar value problem is solved to enforce the manufacturing constraint. In Ref. [2], the pseudo light approach was proposed for the level-set approach. In Ref. [3], the design variables in two-dimensional domain are reduced to a vector to consider the manufacturing constraint. The present approach considers this issue without solving extra physics problem to impose the manufacturing constraint and maintaining the design variables in topology optimization. In this approach, the shadow filter mimics shadows or X-rays in a TO framework. Before explaining the shadow density filter, the geometrical requirements for cast or injection processed need to be discussed. In casting, molten materials are poured into a mold and solidified into the shape of the mold [36,37]. Different casting processes have been introduced based on how the mold is made and how the metal is forced into the mold. Gravity is the most common approach to fill the mold with melted materials, but it is also viable to use centrifugal force or pressure injection. In some cases, undercut geometries at the surfaces can result in voids inside the product, as illustrated in Fig. 1. Note that the present voids or "air pockets" in the injection molding manufacturing process are actually regarded as defects that limit the manufacturing feasibility [36]. The parting direction or line in Fig. 1 should also be considered in the design process. We should consider these aspects during the engineering design, which are important issues in structural optimization to consider during the optimization process. The geometrical constraints are difficult to impose as they are formulated locally [1,2,34,36,38].

A Shadow Density Filtering for One Material Design. For a simple component or design, it relatively simple to identify, modify, and manufacture some unwanted undercut or inter void part. However, in a complex manifold design with nonempty, smooth, a strongly pseudoconvex boundary, it is challenging to identify the features, modify them, and manufacture the part while satisfying the constraint without sacrificing performance. From an optimization point of view, this is ironic because the structure is optimized, but its performance would be sacrificed for manufacturing. Therefore, a rigorous approach is required to impose these constraints. In Ref. [1], the virtual scalar value problem is solved to enforce the manufacturing constraint. In Ref. [2], the pseudo light approach was proposed for the level-set approach. In Ref. [3], the design variables in two-dimensional domain are reduced to a vector to consider the manufacturing constraint. Although the term of the virtual light was used in their studies, they solved the scalar problem (virtual heat flow) to implement the concept.

By inspired by the innovative researches in Refs. [1–3], we also sought to realize the shadowing process in the density filtering approach. Consider any opaque object absorbing light and

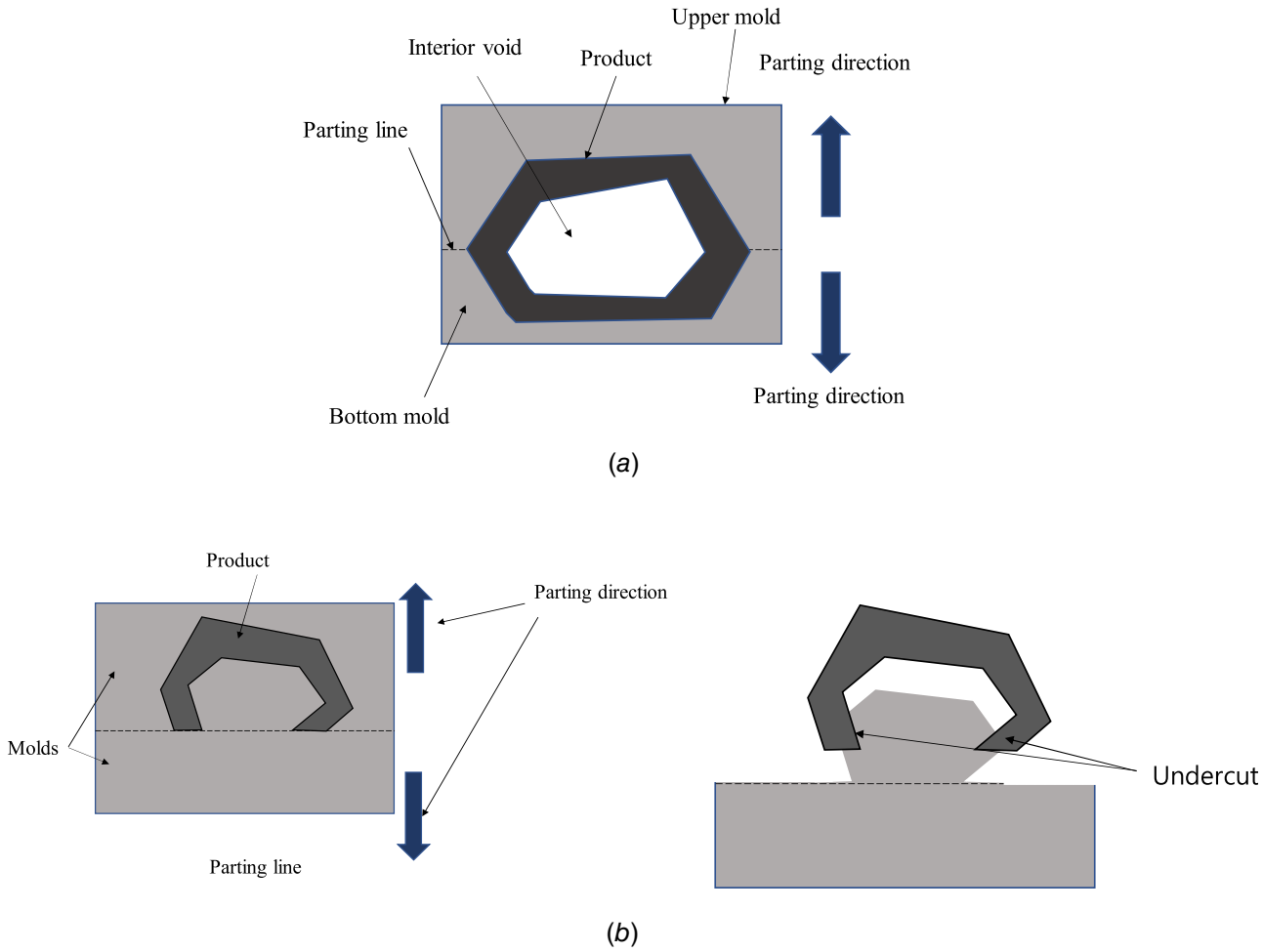

Fig. 1 Parting line (a dividing line between a cavity and a core plate of a mod), interior void, and undercut

producing a shadow (comparative darkness given by shelter from direct light). There is a dark area called the shadow, where light is blocked by an opaque object. The image of the cross section is a two-dimensional silhouette or a projection of the opaque object blocking the light. Shadow shapes vary depending on the type of lights. The gradient or variation of the image can be obtained depending on the absorption ratios. One interesting and important aspect of this shadow phenomenon is that the formed shadow changes depending on the viewing direction. The emitted light can capture the outer boundary of the object in the projecting direction of the light. Our idea is to simulate this shadowing with parallel propagating light or a point light source far from the product in TO to consider the manufacturability. However, we do not propose computationally solving the light path, as this increases the computational time. Rather, we propose simulating the absorbing process to produce a shadow image or the projection of objects. A similar phenomenon can be found in X-ray imaging in an orthopedic hospital. X-ray imaging is captured by emitting a beam of high energy electrons passing through patient toward a sheet of photographic film. We proposed this concept as a density filter in TO.

To use this shadowing technique in TO, we noticed that we can regard the design variables defined at every element as opaque objects. For example, if one design variable is 1 for one element, the parallel light cannot penetrate. If the design variable is 0, then the light can penetrate. The design variables were between zero and one, and some absorption or the attenuation happens at the element. After penetration of the light, the design variable of the neighboring element determines the absorption ratio and the intensity of the light, which also decreased further. If we repeat this process, we can obtain a shadow image at the end of the object. To the best of our knowledge, this direct application of the shadow or a related concept has not been tried yet before this research.

To simulate the shadowing, this research considers the linear absorption relationship χ between the design variable, which varies from 0 to 1. In a two-dimensional domain, the light absorption at a single spatial point can be defined as follows:

Light absorption function:

$$\chi(\gamma_{i,j}) = 1 - \gamma_{i,j} \text{ (any decaying function possible)} \tag{29}$$

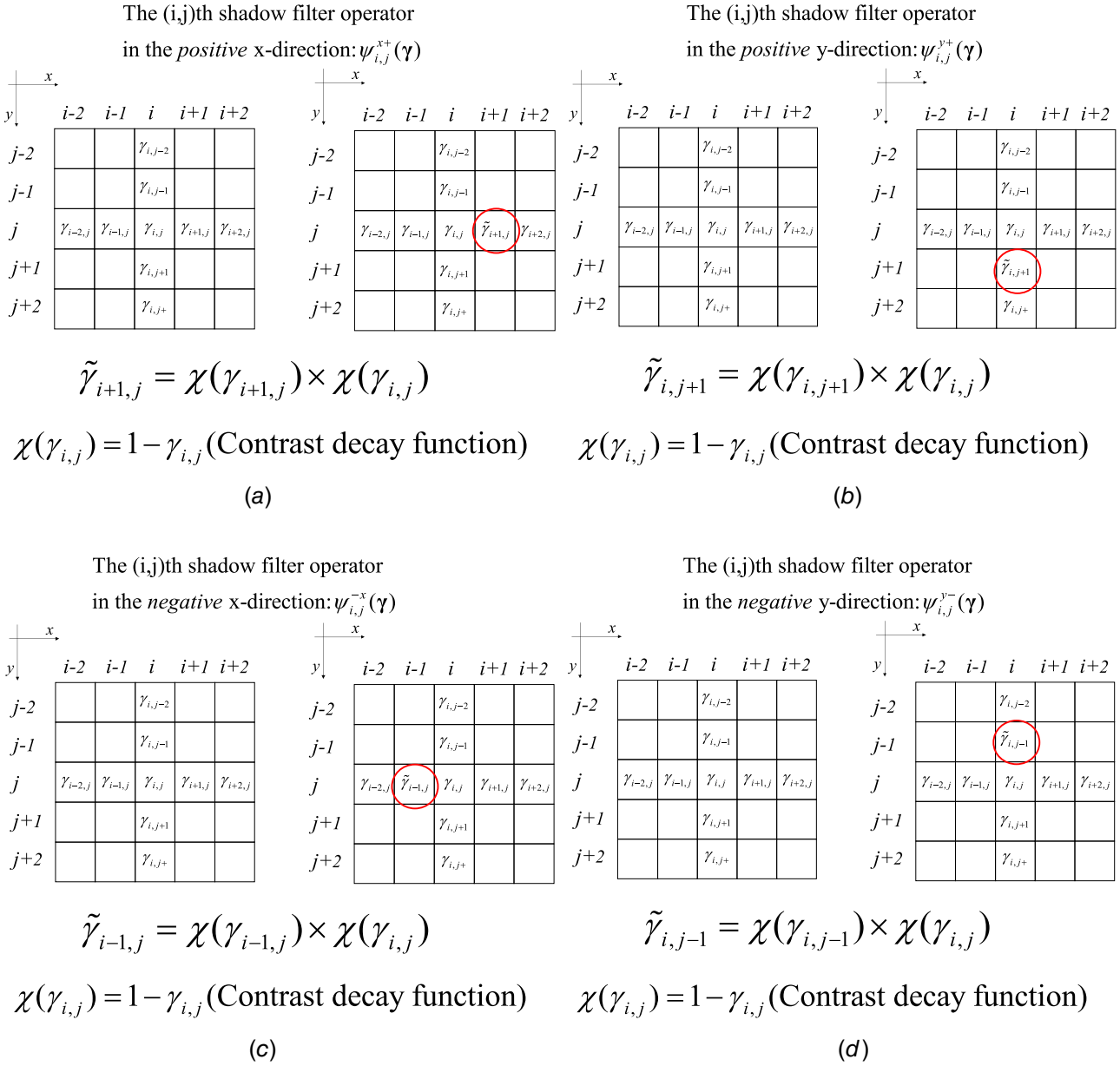

Fig. 2 Elementary shadow operators in the four directions

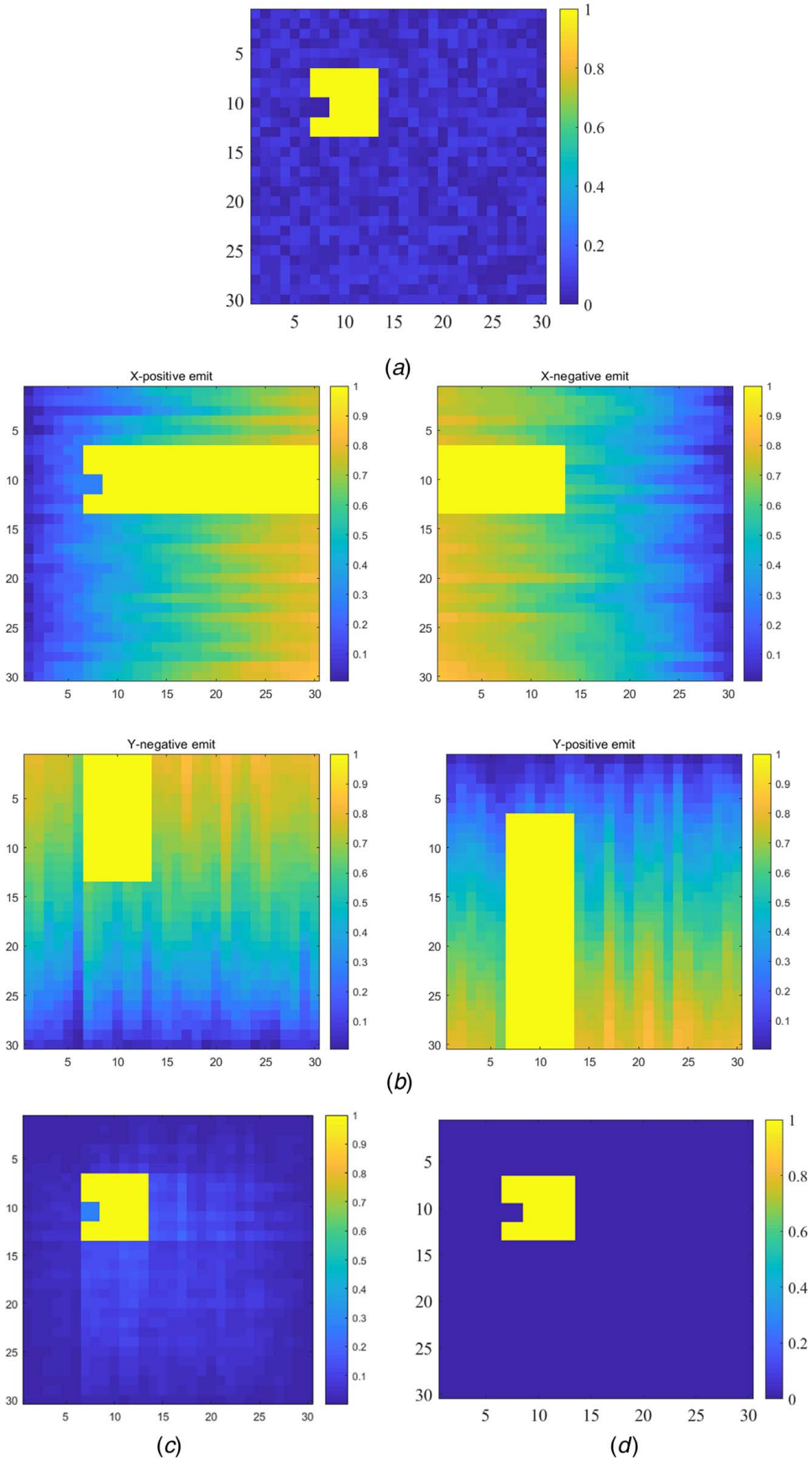

Fig. 3 An example of the shadow filters from (39)–(42): (*a*) an original image, (*b*) the shadows of the image, (c) the combination of the shadow images $\tilde{\gamma} = \Phi(\gamma)$, and (*d*) a projected value of $\tilde{\gamma}$ using the *s*-shape sigmoid function reported in Refs. [21,22] ($\tilde{\gamma} = 1/(1 + \exp(a(\Phi(\gamma) - b)))$, $a = -100$, $b = 0.5$)

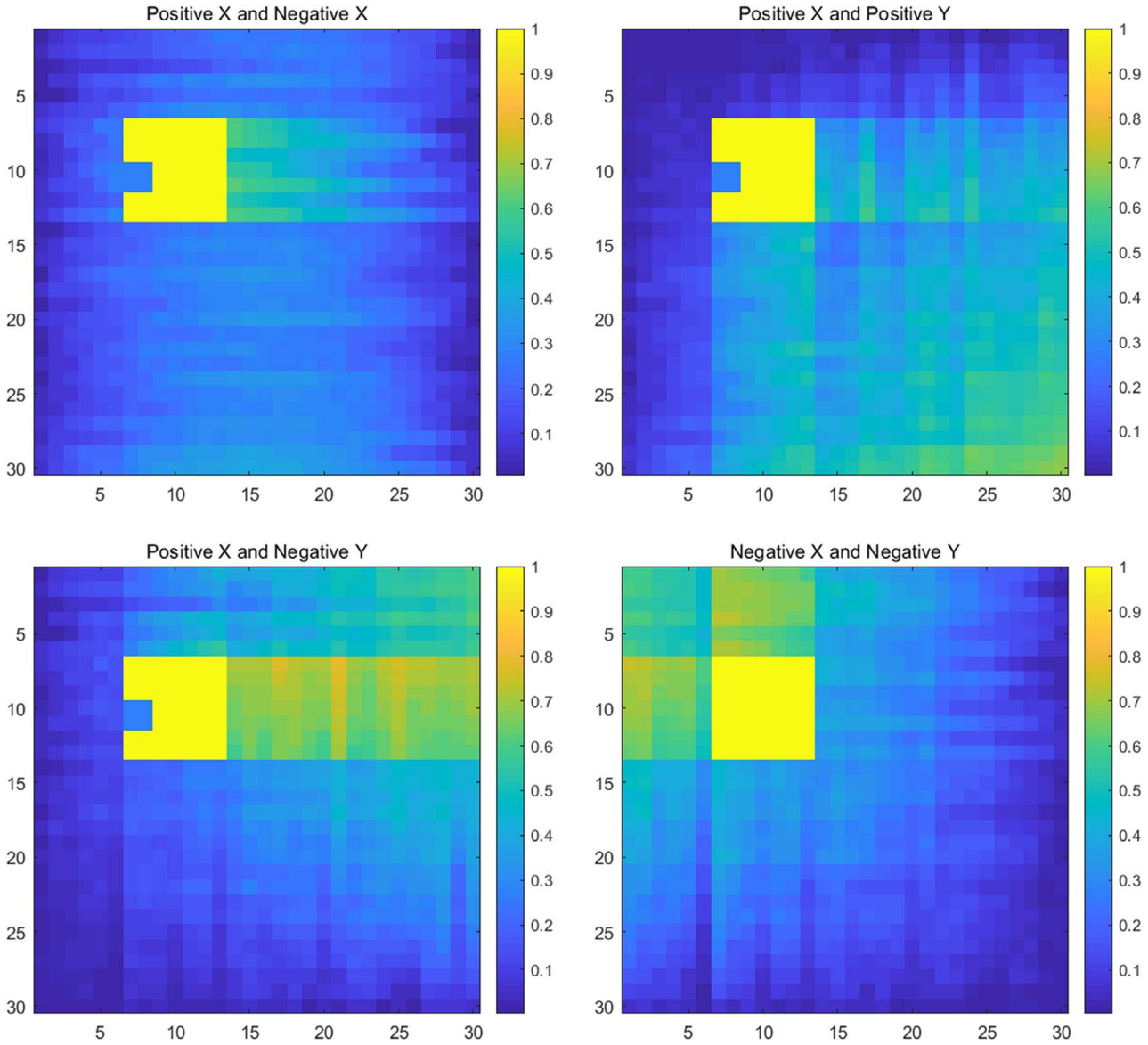

Fig. 4 Some combinations of the shadow filters of the structure in Fig. 3(a)

where the (i,j)th design variable is denoted by $\gamma_{i,j}$ and the decaying function is denoted by χ. When $\gamma_{i,j}$ is one, $\chi(\gamma_{i,j})$ becomes zero and if $\gamma_{i,j}$ is zero, $\chi(\gamma_{i,j})$ becomes one. Then, we can consider the light in the positive x direction, in the negative x direction, in the positive y direction and in the negative y direction. We can define the following unit operators simulating the decrease in the light intensity.

Light absorption:

$$\psi_{i,j}^{x+}(\boldsymbol{\gamma}) = \begin{cases} \gamma_{i,j} \text{ in all elements except } (i+1,j) \text{ element} \\ \tilde{\gamma}_{i+1,j} \text{ for } (i+1,j) \text{ elements } \tilde{\gamma}_{i+1,j} = \chi(\gamma_{i+1,j}) \times \chi(\gamma_{i,j}) \end{cases} \tag{30}$$

Light absorption:

$$\psi_{i,j}^{x-}(\boldsymbol{\gamma}) = \begin{cases} \gamma_{i,j} \text{ in all elements except } (i-1,j) \text{ element} \\ \tilde{\gamma}_{i-1,j} \text{ for } (i-1,j) \text{ elements } \tilde{\gamma}_{i-1,j} = \chi(\gamma_{i-1,j}) \times \chi(\gamma_{i,j}) \end{cases} \tag{31}$$

Light absorption:

$$\psi_{i,j}^{y+}(\boldsymbol{\gamma}) = \begin{cases} \gamma_{i,j} \text{ in all elements except } (i,j+1) \text{ element} \\ \tilde{\gamma}_{i,j+1} \text{ for } (i,j+1) \text{ elements } \tilde{\gamma}_{i,j+1} = \chi(\gamma_{i,j+1}) \times \chi(\gamma_{i,j}) \end{cases} \tag{32}$$

Light absorption:

$$\psi_{i,j}^{y-}(\boldsymbol{\gamma}) = \begin{cases} \gamma_{i,j} \text{ in all elements except } (i,j-1) \text{ element} \\ \tilde{\gamma}_{i,j-1} \text{ for } (i,j-1) \text{ elements } \tilde{\gamma}_{i,j-1} = \chi(\gamma_{i,j-1}) \times \chi(\gamma_{i,j}) \end{cases} \tag{33}$$

Here, the light absorption ratio at the (i,j)th cell is denoted by $\psi_{i,j}^{(\circ)}$, where $\circ$ indicates the direction of the light. At the boundary, the light absorption coefficients are defined as follows.

Light absorption:

$$\psi_{1,j}^{x+}(\boldsymbol{\gamma}) = \begin{cases} \gamma_{i,j} \text{ in all elements except } (1,j) \text{ element} \\ \tilde{\gamma}_{1,j} = \chi(\gamma_{1,i}) \end{cases} \tag{34}$$

Light absorption:

$$\psi_{nelx,j}^{x-}(\boldsymbol{\gamma}) = \begin{cases} \gamma_{i,j} \text{ in all elements except } (nelx,j) \text{ element} \\ \tilde{\gamma}_{nelx,j} = \chi(\gamma_{nelx,j}) \end{cases} \tag{35}$$

Light absorption:

$$\psi_{i,1}^{y+}(\boldsymbol{\gamma}) = \begin{cases} \gamma_{i,j} \text{ in all elements except } (i,1) \text{ element} \\ \tilde{\gamma}_{i,1} = \chi(\gamma_{i,1}) \end{cases} \tag{36}$$

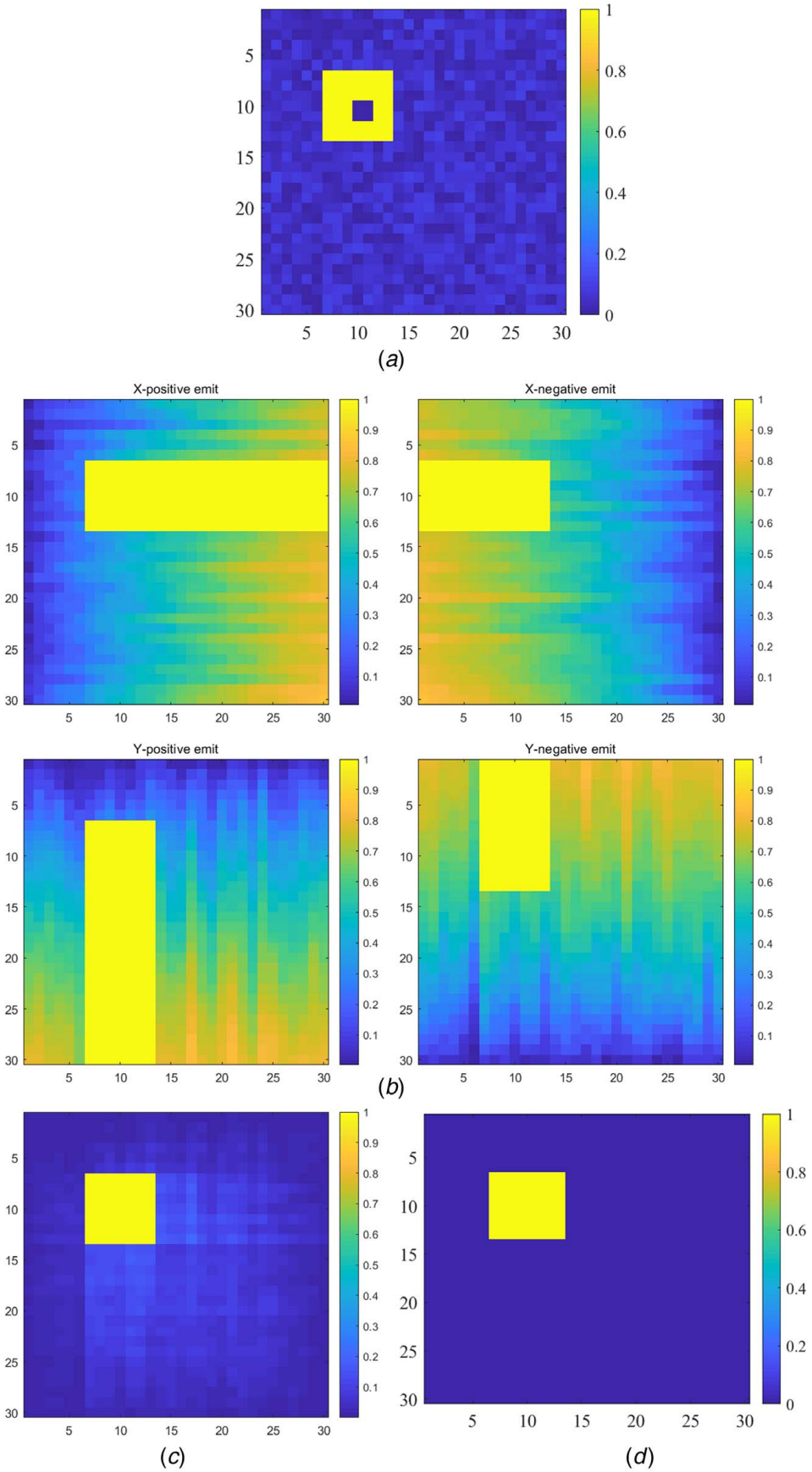

Fig. 5 A second example of the shadow filters from (39)–(42): (*a*) an original image, (*b*) the shadows of the image, (c) the combination of the shadow images $\tilde{\gamma} = \Phi(\gamma)$, and (*d*) a projected value of $\tilde{\gamma}$ using the *s*-shape sigmoid function reported in Refs. [21,22] ($\tilde{\gamma} = 1/(1 + \exp(a(\Phi(\gamma) - b)))$, $a = -100$, $b = 0.5$)

Light absorption:

$$\psi^{y-}_{i,nely}(\boldsymbol{\gamma}) = \begin{cases} \gamma_{i,j} \text{ in all elements except } (i, nely) \text{ element} \\ \tilde{\gamma}_{i,nely} = \chi(\gamma_{i,nely}) \end{cases} \tag{37}$$

Then, we can define the combinations of the above coefficients repeatedly to construct the shadow images, which are used to determine the physical density in the finite element simulation

$$\begin{aligned} \Upsilon^{+}_{i}(\boldsymbol{\gamma}) &= \psi^{x+}_{nelx,i}(\psi^{x+}_{nelx-1,i}(\psi^{x+}_{nelx-2,i}(\psi^{x+}_{nelx-3,i}(\cdots\psi^{x+}_{2,i}(\psi^{x+}_{1,i}(\boldsymbol{\gamma})))))) \\ \Upsilon^{-}_{i}(\boldsymbol{\gamma}) &= \psi^{x-}_{nelx,i}(\psi^{x-}_{1,i}(\psi^{x-}_{2,i}(\psi^{x-}_{3,i}(\cdots\psi^{x-}_{nelx-1,i}(\psi^{x-}_{nelx,i}(\boldsymbol{\gamma})))))) \\ \Xi^{+}_{j}(\boldsymbol{\gamma}) &= \psi^{y+}_{j,nely}(\psi^{x+}_{j,nely-1}(\psi^{x+}_{j,nely-2}(\psi^{x+}_{j,nely-3}(\cdots\psi^{x+}_{j,2}(\psi^{x+}_{j,1}(\boldsymbol{\gamma})))))) \\ \Xi^{-}_{j}(\boldsymbol{\gamma}) &= \psi^{y+}_{j,1}(\psi^{x+}_{j,2}(\psi^{x+}_{j,3}(\psi^{x+}_{j,4}(\cdots\psi^{x+}_{j,nely-1}(\psi^{x+}_{j,nely}(\boldsymbol{\gamma})))))) \end{aligned} \tag{38}$$

X-positive light:

$$\tilde{\boldsymbol{\gamma}} = \Phi^{x+}(\boldsymbol{\gamma}) \equiv [(1-\Upsilon^{+}_{1}(\boldsymbol{\gamma}))(1-\Upsilon^{+}_{2}(\boldsymbol{\gamma}))\cdots(1-\Upsilon^{+}_{nely}(\boldsymbol{\gamma}))] \tag{39}$$

X-negative light:

$$\tilde{\boldsymbol{\gamma}} = \Phi^{x-}(\boldsymbol{\gamma}) \equiv [(1-\Upsilon^{-}_{1}(\boldsymbol{\gamma}))(1-\Upsilon^{-}_{2}(\boldsymbol{\gamma}))\cdots(1-\Upsilon^{-}_{nely}(\boldsymbol{\gamma}))] \tag{40}$$

Y-positive light:

$$\tilde{\boldsymbol{\gamma}} = \Phi^{y+}(\boldsymbol{\gamma}) \equiv [(1-\Xi^{+}_{1}(\boldsymbol{\gamma}))(1-\Xi^{+}_{2}(\boldsymbol{\gamma}))\cdots(1-\Xi^{+}_{nely}(\boldsymbol{\gamma}))] \tag{41}$$

Y-negative light

$$\tilde{\boldsymbol{\gamma}} = \Phi^{y-}(\boldsymbol{\gamma}) \equiv [(1-\Xi^{-}_{1}(\boldsymbol{\gamma}))(1-\Xi^{-}_{2}(\boldsymbol{\gamma}))\cdots(1-\Xi^{-}_{nely}(\boldsymbol{\gamma}))] \tag{42}$$

We can also combine the above operators for an engineering point of view. For instance, the following expresses the combination of the filters (Fig. 2)

$$\begin{aligned} \tilde{\boldsymbol{\gamma}} = \Phi_{All}(\boldsymbol{\gamma}) &\equiv \Phi^{x+}(\boldsymbol{\gamma})\Phi^{x-}(\boldsymbol{\gamma})\Phi^{y+}(\boldsymbol{\gamma})\Phi^{y-}(\boldsymbol{\gamma}) \\ &= [(1-\Upsilon^{+}_{1}(\boldsymbol{\gamma}))(1-\Upsilon^{+}_{2}(\boldsymbol{\gamma}))\cdots(1-\Upsilon^{+}_{nely}(\boldsymbol{\gamma}))] \\ &\times [(1-\Upsilon^{-}_{1}(\boldsymbol{\gamma}))(1-\Upsilon^{-}_{2}(\boldsymbol{\gamma}))\cdots(1-\Upsilon^{-}_{nely}(\boldsymbol{\gamma}))] \\ &\times [(1-\Xi^{+}_{1}(\boldsymbol{\gamma}))(1-\Xi^{+}_{2}(\boldsymbol{\gamma}))\cdots(1-\Xi^{+}_{nely}(\boldsymbol{\gamma}))] \\ &\times [(1-\Xi^{-}_{1}(\boldsymbol{\gamma}))(1-\Xi^{-}_{2}(\boldsymbol{\gamma}))\cdots(1-\Xi^{-}_{nely}(\boldsymbol{\gamma}))] \end{aligned} \tag{43}$$

To illustrate the defined operators, Figs. 3 and 4 show two illustrative structures and their shadows made by the described filters. A dimple is inserted in Fig. 3(*a*) at the left side of the structure, which can be regarded as an undercut. Figure 3(*b*) illustrates the shadow images of the four filters, and their combination is shown in Fig. 3(*c*). It is also possible to witness some strong blur marks at the shadow image at the left of Fig. 3(*c*) due to the light attenuation. To make the image clear, it is possible to introduce the *s*-shaped function on the right of Fig. 3(*c*) [21,22]. Figure 4 shows the combination applications of the shadow filters. This example shows that it is possible to combine the shadow filter in each direction. Figure 5 shows another example with a void. As stated before, the application of the shadow filter can capture the outline of the structure. The present shadow filter may be extended to the overhang filters in topology optimization. Rather than observing adjacent and diagonally adjacent element, this shadow filter can be interpreted as imposing the max operator to impose the manufacturing constraint. By limiting the considered elements, this approach may be extended to consider the overhang constraints in topology optimization.

The Inclined Shadow Filter. The above shadow density filter is defined along the parallel *x*- or *y*-directions. By changing the direction of the virtual light, it is possible to define the inclined molding direction. To achieve this, this research proposes to rotate the image of the design variables and apply the above shadow operators. To

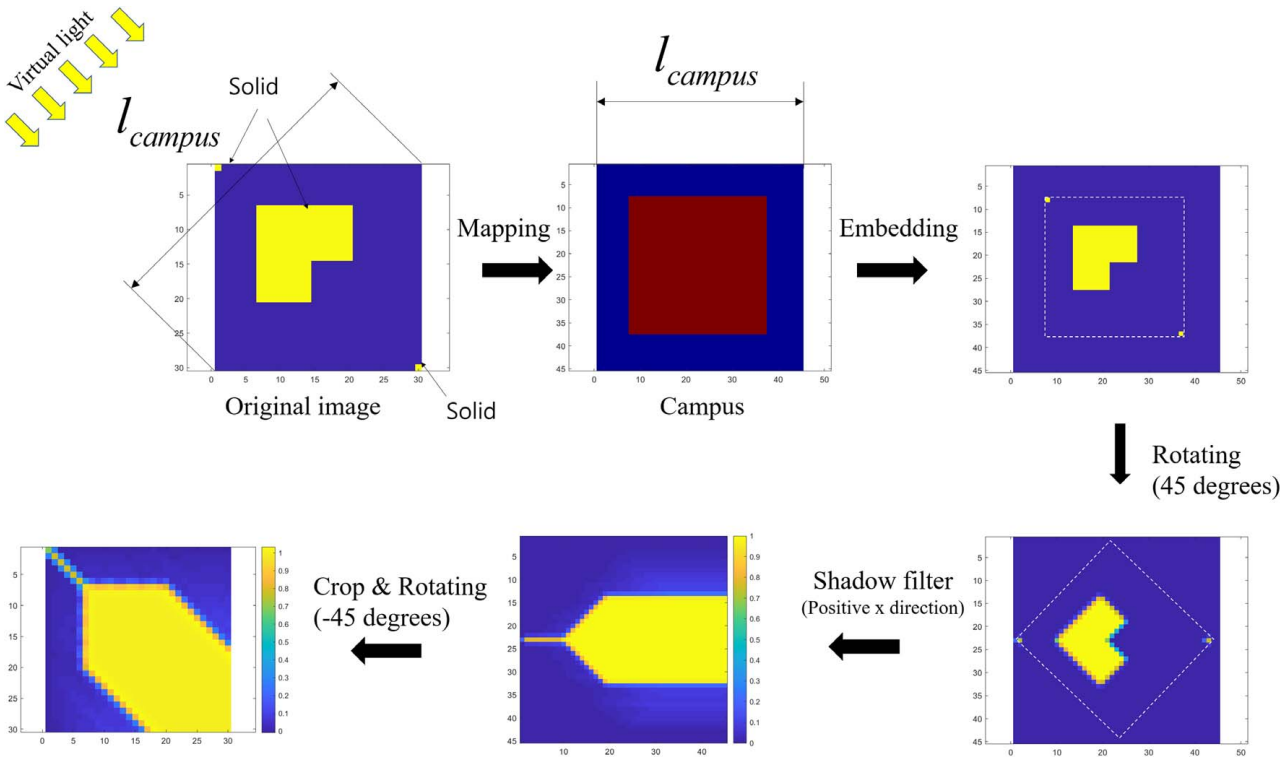

Fig. 6 The concept of the inclined shadow filter using the linear mapping (The original image is embedded in a larger domain (Campus) and it is rotated considering the direction of the virtual light. The image applied with the shadow filter is cropped and rotated to obtain the shadowed image.)

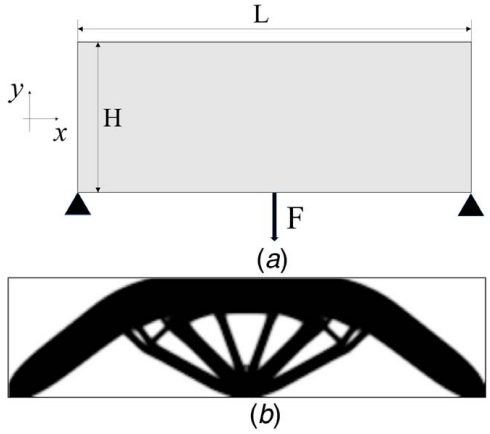

Fig. 7 Problem definition and an optimal design using the SIMP approach ($L = 2$ m, $H = 1$ m, $F = 1$ N, $E = 1$ N/m^2, $\nu = 0.3$, $c = 0.4517$ J, 50% mass constraint)

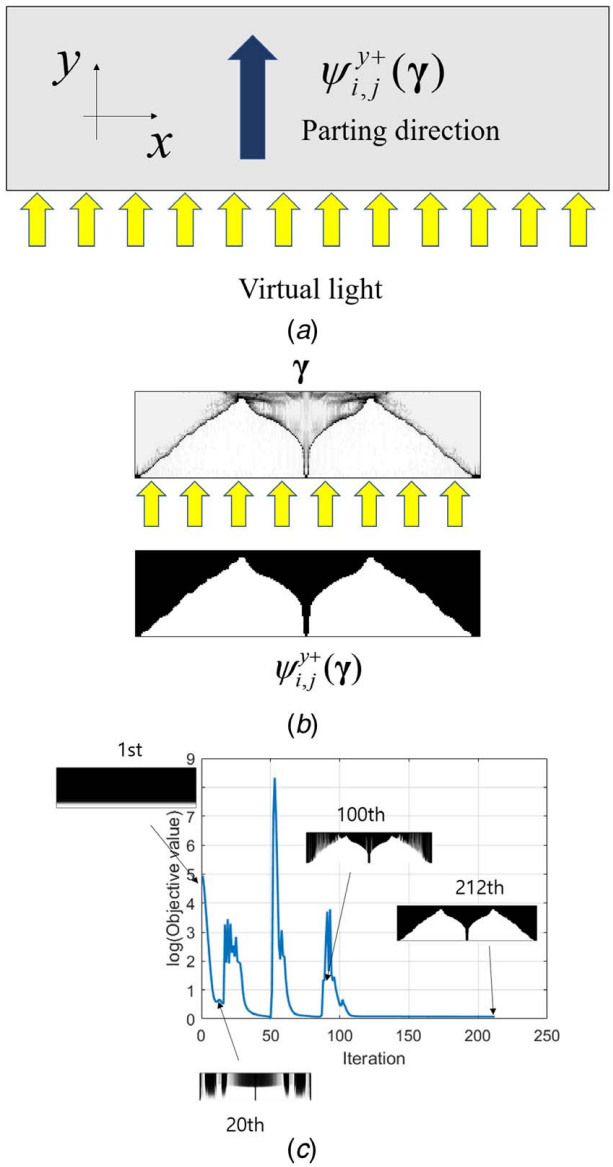

Fig. 8 An optimization result with the shadow filter ($\psi_{i,j}^{y+}(\gamma)$) (one-way casting)

rotate and interpolate the images, we use the linear mapping function implemented in MATLAB (*imrotate.m*), which allows the differentiable rotating operators. Figure 6 shows an example of the concept of the inclined shadow filter with the 45 deg virtual light.

Sensitivity Analysis of the Shadow Filter. The objective function and the sensitivity value considering any type of density filter can be formulated analytically for the compliance minimization problem. In the shadow density filters developed in (39)–(42), each element filter can be treated by one density filter. For example, let us consider the objective gradient with a shadow filter $\tilde{\boldsymbol{\gamma}} = \Phi^{x+}(\boldsymbol{\gamma})$; in that case, the gradient of the objective function should be computed as follows:

$$\frac{dc}{d\gamma_e} = \frac{dc}{d\tilde{\boldsymbol{\gamma}}}\frac{d\tilde{\boldsymbol{\gamma}}}{d\gamma_e} = \frac{dc}{d\tilde{\boldsymbol{\gamma}}}\frac{d\Phi^{x+}(\boldsymbol{\gamma})}{d\gamma_e}$$
$$= \frac{dc}{d\tilde{\boldsymbol{\gamma}}}\begin{pmatrix}\left[(-\frac{d\Upsilon_1^+(\boldsymbol{\gamma})}{d\gamma_e})(1-\Upsilon_2^+(\boldsymbol{\gamma}))\cdots(1-\Upsilon_{nely}^+(\boldsymbol{\gamma}))\right]+\\ \left[(1-\Upsilon_1^+(\boldsymbol{\gamma}))(-\frac{d\Upsilon_2^+(\boldsymbol{\gamma})}{d\gamma_e})\cdots(1-\Upsilon_{nely}^+(\boldsymbol{\gamma}))\right]+\\ \cdots\\ \left[(1-\Upsilon_1^+(\boldsymbol{\gamma}))(1-\Upsilon_2^+(\boldsymbol{\gamma}))\cdots(-\frac{d\Upsilon_{nely}^+(\boldsymbol{\gamma})}{d\gamma_e})\right]+\end{pmatrix} \quad (44)$$

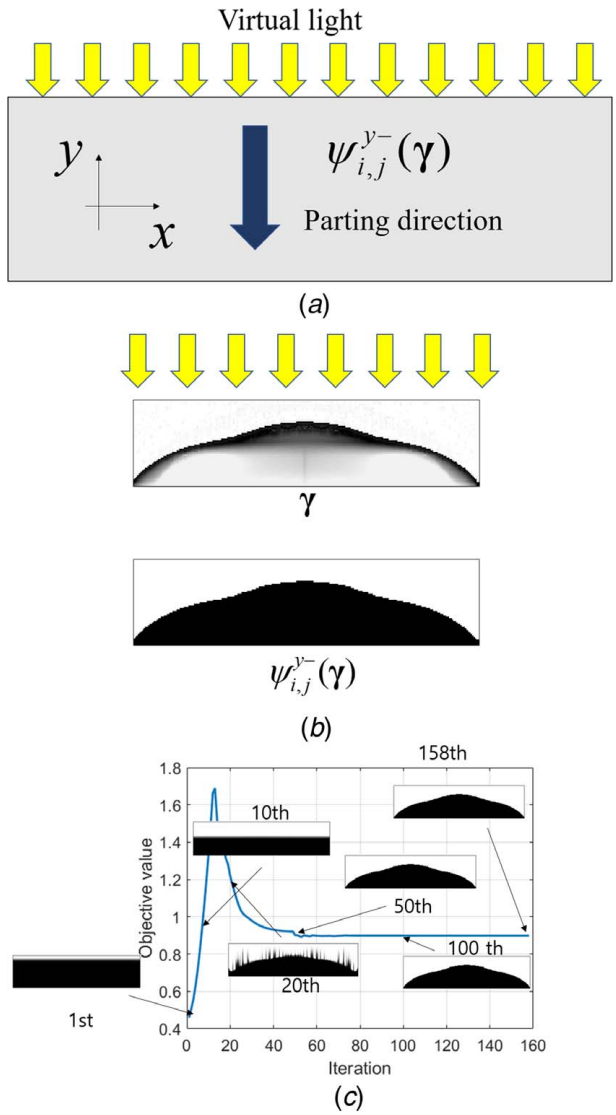

Fig. 9 An optimization results with the shadow filter ($\psi_{i,j}^{y-}(\gamma)$) (one-way casting)

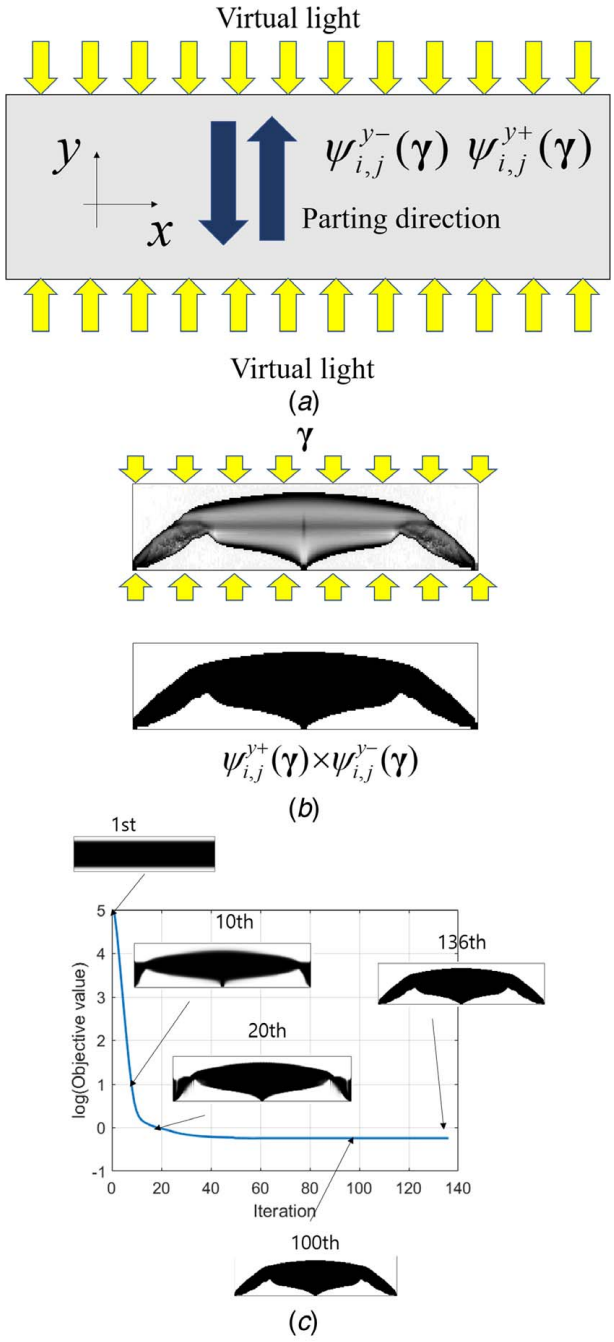

Fig. 10 An optimization result with the shadow filter ($\psi_{i,j}^{y+}(\gamma)\times\psi_{i,j}^{y-}(\gamma)$)

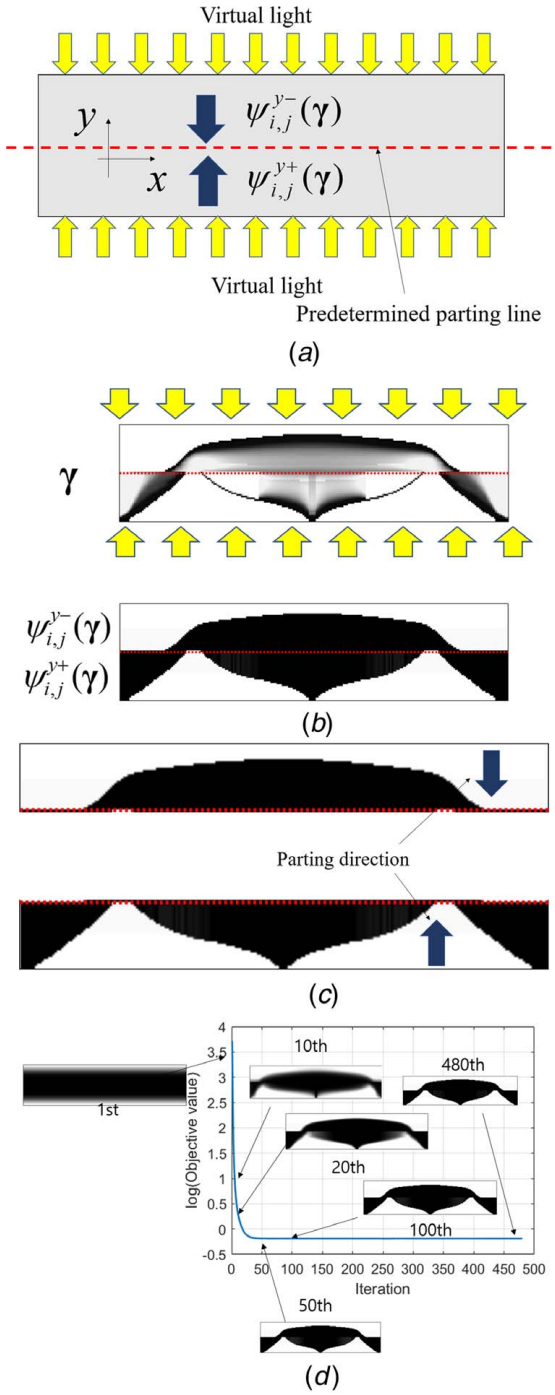

Fig. 11 Two parts with different parting directions: (*a*) the problem definition, (*b*) an optimal design, (*c*) two parts, and (*d*) an optimization history

The differentiations of $\Upsilon_i(\boldsymbol{\gamma})$ should be obtained by considering Eq. (38). The directional properties of the shadow can be used to reduce the computation time. In other words, the perturbations of the design domain influenced the filtered design variables in the direction of the shadow only.

An Extension of the Shadow Density Filtering for Multiple Material Design. The application of the shadow density filter can be extended for multiple materials. As an example, we can consider a structural design with two materials, and we can assume the molding condition for only one material. In that case, we reformulated the optimization problem (4) as follows:

$$\underset{\boldsymbol{\gamma}=[\boldsymbol{\gamma}_1,\boldsymbol{\gamma}_2]}{\text{Min}}\ c=\mathbf{F}^{\mathrm{T}}\mathbf{U}$$

subject to

$$V_1(\tilde{\boldsymbol{\gamma}}_1)\le\bar{V}_1 \qquad (45)$$

$$V_2(\boldsymbol{\gamma}_2)\le\bar{V}_2$$

$$\mathbf{K}([\tilde{\boldsymbol{\gamma}}_1,\boldsymbol{\gamma}_2])\mathbf{U}=\mathbf{F},\ \tilde{\boldsymbol{\gamma}}_1=\Phi(\boldsymbol{\gamma}_1)$$

Φ:Shadow filter

$$\mathbf{k}_e=\tilde{\gamma}_1^n(1-\gamma_2^n)\mathbf{k}_e^1+\gamma_2^n(1-\tilde{\gamma}_1^n)\mathbf{k}_e^2 \qquad (46)$$

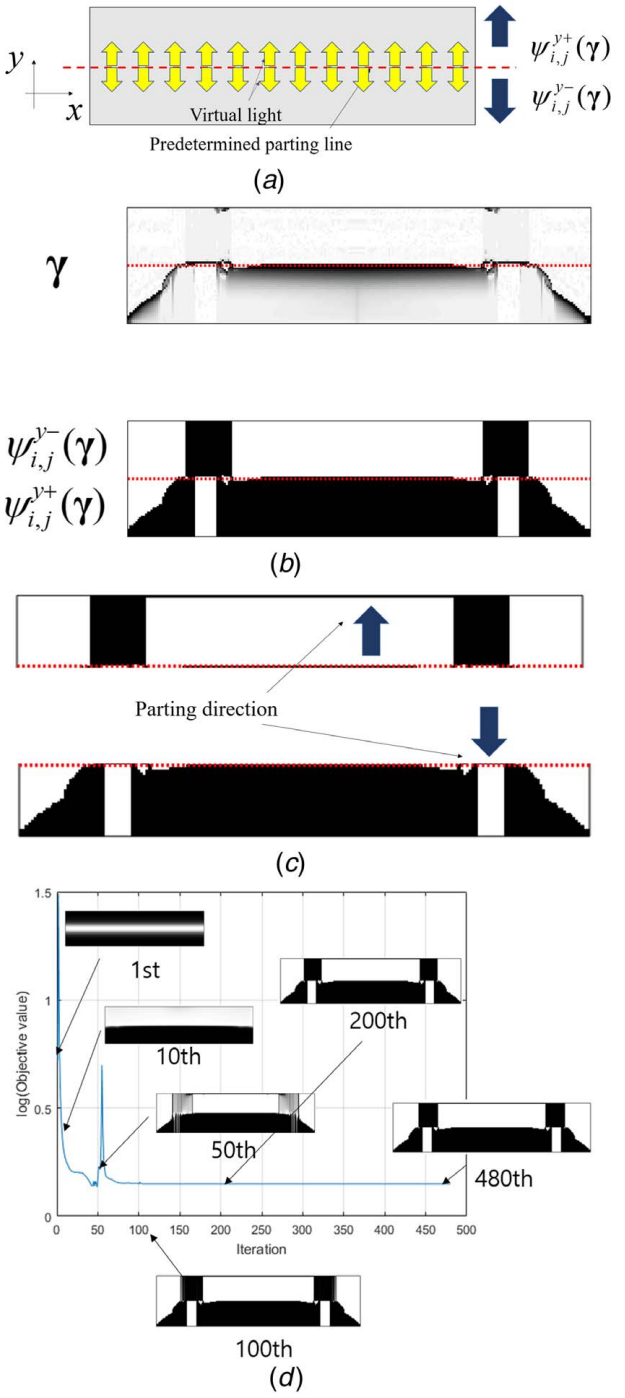

Fig. 12 Two parts with different parting directions: (*a*) the problem definition, (*b*) an optimal design, (c) two parts, and (*d*) an optimization history

Here, the upper limits of the first and the second materials are $\bar{V}_1$ and $\bar{V}_2$, respectively. The finite elements with the first Young's modulus and the second Young's modulus are denoted by $\mathbf{k}_e^1$ and $\mathbf{k}_e^2$, respectively. The two variables are assigned to one finite element, and only the first parameter is filtered by the shadow density filter. With this extension, it is possible to design a molding structure with two materials, and the shadow density filter is imposed only for one material.

Shadow Cap Filter—A Heuristic Filtering Scheme. As discussed before, the shadow density filter in Sec. 3.1 can be regarded as a new density filter. However, the variables filtered by this shadow filter can be heuristically reused during an optimization process. In other words, the design variables are re-set by the variables filtered in this filter. Although it is a heuristic filter from a mathematical point of view, it can be easily used in the framework of an existing optimization framework to impose manufacturability by just replacing the design variables with the filtered ones.

Optimization Results

To illustrate the characteristics of the present shadow filter, several examples are solved, and the optimization results obtained without considering the manufacturing feature are compared. The first example is a rectangular box design, which was solved in some relevant studies to demonstrate that the molding constraint is achieved. In addition, the application of multiple materials is presented with the first example. The second example is also a rectangular box with a simple clamped boundary condition and is used to demonstrate the application of the shadow filters in a two-dimensional problem. The heuristic design variable update scheme was also tested in the second example. Note that the consistent sensitivity analysis in (6) and (7) has been used for all the examples except the example in Sec. 3.3. The example in Sec. 3.3 is to demonstrate that the present filter also can be used as the postprocessing filter during or after the optimization. Both examples assume a thickness of 1 and some idealized design domains. The boundary conditions were applied to illustrate the characteristics of the present filters. The heat dissipation structure design and the mechanism design with fluid–structure interaction are also considered to see the effect of the manufacturing constraint in topology optimization. A three-dimensional problem is considered in the third example. Like the two-dimensional examples, the manufacturing constraints were imposed successfully. All the codes were implemented in the MATLAB with the method of moving asymptotes optimizer. The maximum optimization iteration is set to 500 with the relative objective convergence is set to 0.001. The a parameter of the sigmoid function is set -10 and increased two times every 50 iterations up to -100 and b is set to 0.5 for all the present examples. Note that the optimization results are the plots with the filtered physical density values. All the examples show that the manufacturing constraints can be imposed successfully depending on the combinations of the filters. Note that we do not insert a constraint in the present shadow filter, rather the linear filter that mimics the shadowing is inserted as a density filter. Some numerical approaches of our previous studies using the wavelet-based topology optimization and the s-shape function approach with some variations are applied to enhance the optimization convergence [21,22].

Example 1: Two-Dimensional Compliance Minimization Problem. In the first numerical example, we considered the compliance minimization problem in Fig. 7. This two-dimensional problem with the center point load was researched to study the manufacturing constraints in topology optimization. The design domain was discretized into 120×60 elements, and a 50% mass limit. Using the compliance minimization problem with the density-based approach, we can easily obtain the design in Fig. 7(*b*), which is optimized by the SIMP (the penalization of SIMP = 3) with $c = 0.4517$ J. Note that it is impossible to manufacture this part using molding in the x- and y-directions. Then, the shadow filters in the y-positive direction in Fig. 8, the y-negative direction in Fig. 9, the y-positive and negative directions simultaneously in Fig. 10 and the shadow filters with the parting line at the center with the opposite directions in Figs. 11 and 12. The M-shape design can be obtained with the light in the y-positive direction from the bottom line in Fig. 8. The filter $\psi_{i,j}^{y+}(\boldsymbol{\gamma})$ prohibits internal holes inside the structure. Based on our understanding, this design is fit to the casting manufacturing technique where holes or voids inside the products must be aligned along a single direction (here, the positive direction). Because of the imposed condition with the filter $\psi_{i,j}^{y+}(\boldsymbol{\gamma})$, the compliance or the inverse of the stiffness of the

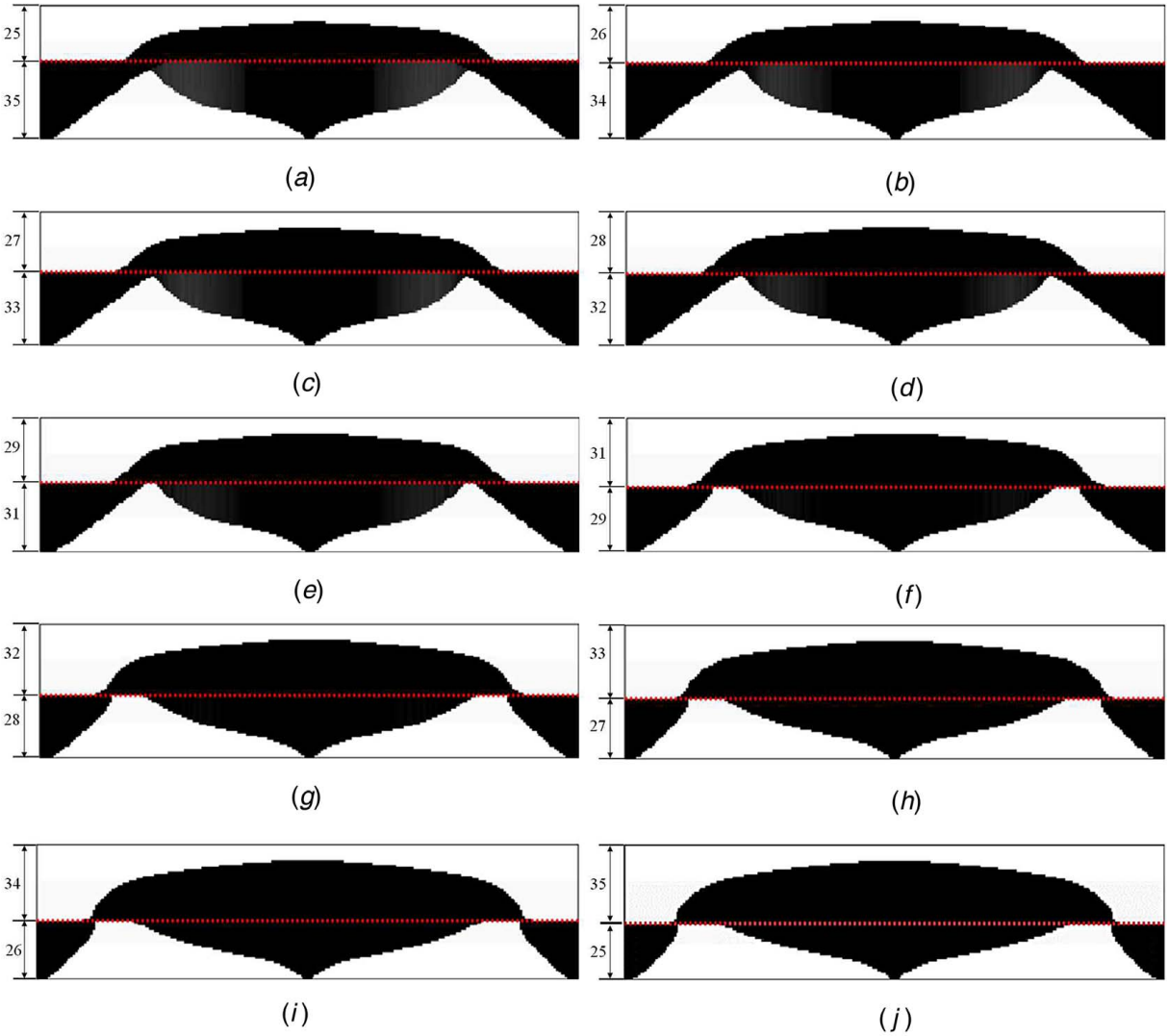

Fig. 13 Effect of the parting line: (*a*) $c = 0.6973$ J, (*b*) $c = 0.6687$ J, (*c*) $c = 0.6687$ J, (*d*) $c = 0.6546$ J, (*e*) $c = 0.6466$ J, (*f*) $c = 0.6607$ J, (*g*) $c = 0.7040$ J, (*h*) $c = 0.7440$ J, (*i*) $c = 0.7606$ J, and (*j*) $c = 0.7802$ J

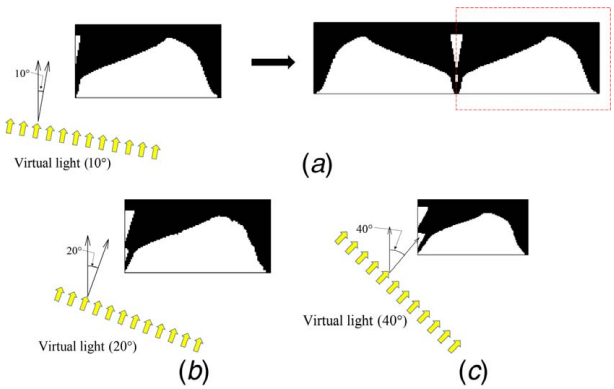

Fig. 14 The optimal layouts with the oblique shadow filter with the half design domain: (*a*) $c = 1.2516$ J, (*b*) $c = 1.2210$ J, and (*c*) $c = 1.0708$ J

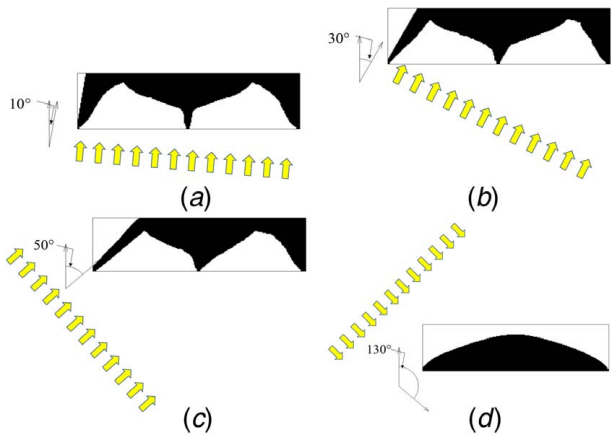

Fig. 15 The optimal layouts with the oblique shadow filter with the whole design domain: (*a*) $c = 2.1411$ J, (*b*) $c = 1.8429$ J, (*c*) $c = 1.5341$ J, and (*d*) $c = 1.6069$ J

structure increases in this example from $c = 0.4517$ J to $c = 1.1949$ J. Some oscillations of the objective function are observed as shown in Fig. 8 especially at the beginning of the optimization process due to the effect of the shadow filter. After some optimization iterations, the stable optimization iterations are observed.

Figure 9 shows an optimal design with the light from the top surface toward the y-negative direction, similar to Fig. 8. The design manufactured by the metal flow toward the y-negative direction

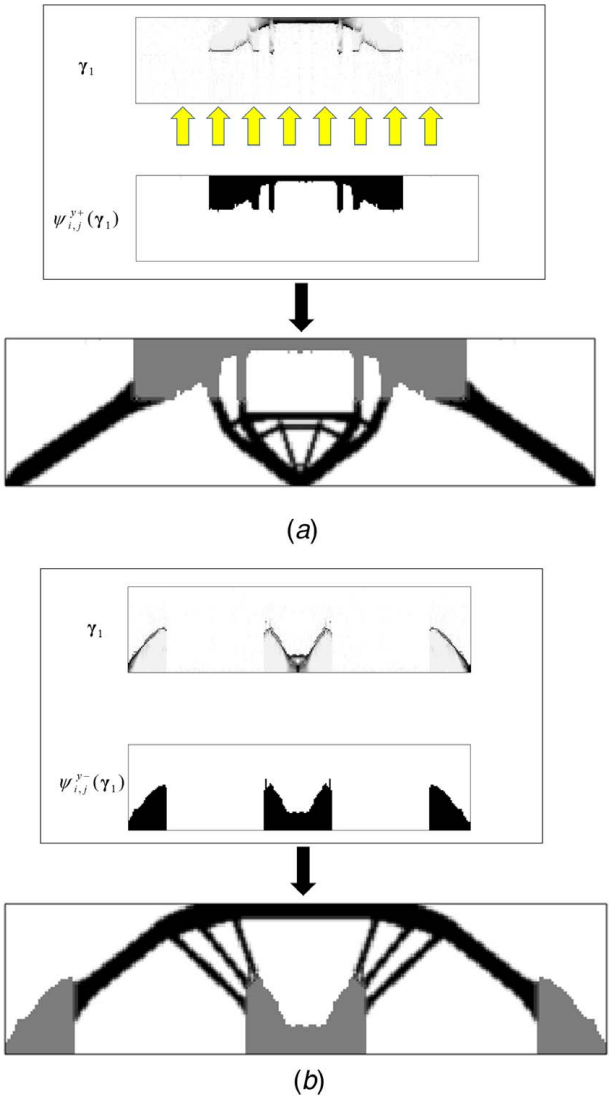

Fig. 16 Two material design (*a*) with $\tilde{\gamma}_1 = \psi^{y+}_{i,j}(\gamma_1)$ and (*b*) with $\tilde{\gamma}_1 = \psi^{y-}_{i,j}(\gamma_1)$ (gray indicates the first design variables filtered by the shadow filter and black indicates the second design variables)

$(\psi^{y-}_{i,j}(\boldsymbol{\gamma}))$ can be obtained without any internal holes. Again, the compliance changed from $c = 0.4517$ J to $c = 0.8984$ J. Figure 10 shows an optimal layout using the two filters $(\psi^{y+}_{i,j}(\boldsymbol{\gamma})$ and $\psi^{y-}_{i,j}(\boldsymbol{\gamma}))$ simultaneously. Comparing some designs, this design can be regarded as the optimized layout obtained by considering the *y*-positive and *y*-negative mold casting. Note that the design in Fig. 10 is made by flowing the melting metal or plastic from the top surface toward the bottom surface and from the bottom surface toward the top surface. In the manufacturing process, it is also possible to manufacture two parts with the opposite flowing directions and join them. It is possible to limit the light and the shadow, as shown in Figs. 11 and 12, to understand this manufacturing process. Figure 13 shows the effect of the parting line. As discussed in Refs. [1,2], the parting line affects the optimal designs and it shows that there will be some optimal parting lines for this problem. This example illustrates that the developed shadow filter can consider this situation. As the consistent sensitivity analysis in (6) and (7) is used, the volume constraint is satisfied for all the examples.

The Oblique Shadow Filter Design. Depending on the engineering problem, it is often necessary to use the inclined molding part. To test this feature developed in Fig. 6, the problem is resolved

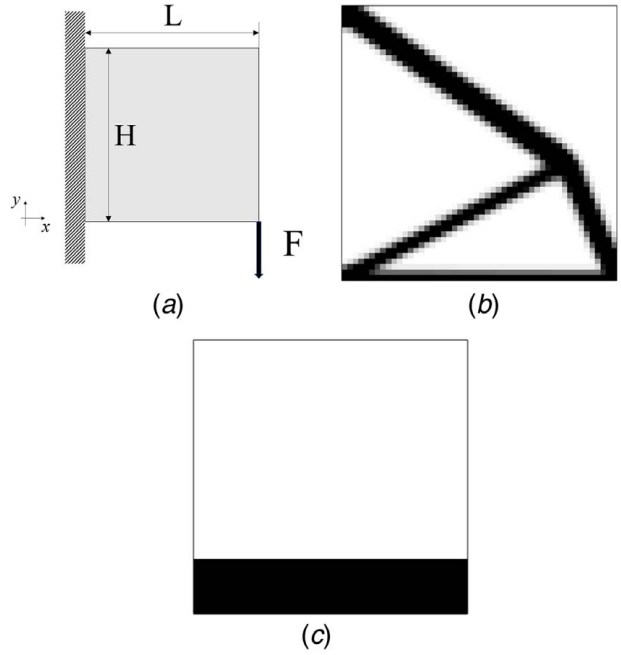

Fig. 17 The optimal design with the shadow filters with a 20% mass constraint with a refined mesh (50 by 50, force = 0.1 N, $E = 1$ N/m^2, $\nu = 0.3$, $L = H = 1$ m): (*a*) problem definition, (*b*) an optimal layout with SIMP ($c = 0.4994$ J), and (c) a reference straight design ($c = 5.1567$ J)

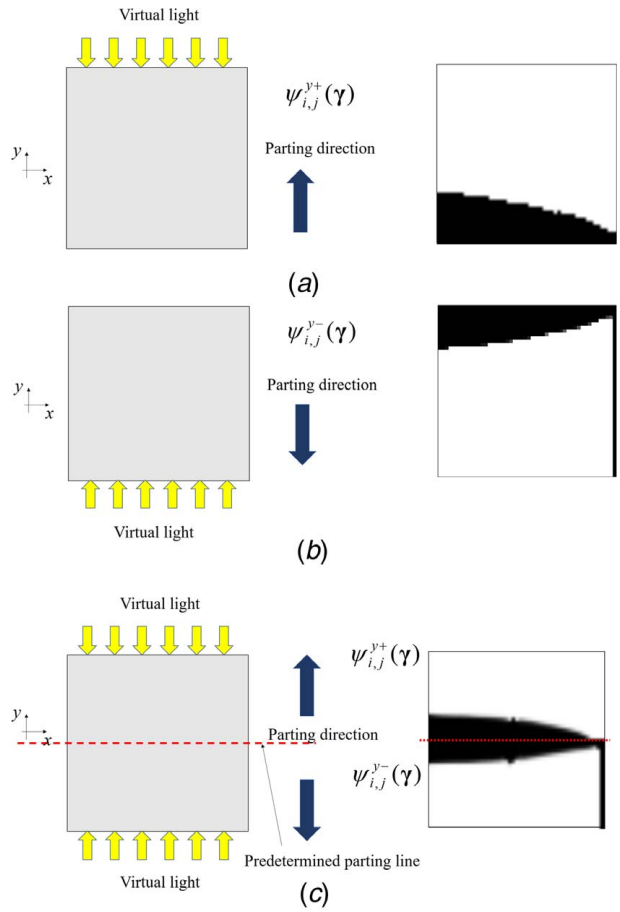

Fig. 18 The optimal designs with the shadow filters: (*a*) $c = 3.3248$ J, (*b*) $c = 5.8360$ J, and (c) $c = 5.7004$ J

by changing the light direction. Note that due to the symmetry of the problem, the half finite element model is solved first in Fig. 14; it is assumed that the left part and the right part are molded and jointed (See Fig. 14(*a*)). By changing the angle to 10, 20, and 40 deg, the present shadow filter successfully provides the optimal layouts. As only the half of the design domain is optimized, internal holes can appear. Therefore, the whole domain is reoptimized with the oblique shadow filter in Fig. 15. As shown, the present shadow filter can impose the manufacturing constraint successfully.

Application for Two Material Design. As formulated, the present shadow filter can also be applied for multi-material design. It is possible to apply the shadow density filter independently. To illustrate this feature, we resolved the above optimization problem with the two materials ($E_2/E_1 = 2$). The shadow filter is only applied for the first material with E_1. The penalization of the SIMP is set to 3 for this example. To avoid the checkerboard, the sensitivity filter was applied for the second design variable. The upper bounds of the masses are set to 15%. Figure 16(*a*) shows the optimal design with $\tilde{\boldsymbol{\gamma}}_1 = \psi_{i,j}^{y+}(\boldsymbol{\gamma}_1)$, and it appears that the second material connects the boundary condition and the loading point. The second part rendered in a gray color can be manufactured by molding. Figure 16(*b*) shows an optimal layout with $\tilde{\boldsymbol{\gamma}}_1 = \psi_{i,j}^{y-}(\boldsymbol{\gamma}_1)$. Because of the imposed manufacturing constraint, the second material appears at the bottom part, and the first material connects the molding parts. The compliances of these designs are similar to each other.

Example 2: Two-Dimensional Rectangular Box Problem. In the next example, the rectangular box problem in Fig. 17 is considered with the application of the shadow filter. We can easily obtain the optimal structure in the compliance minimization problem with the density-based approach, as shown in Fig. 17(*b*). As shown, they are optimal in terms of the objective function, but there are some limitations in manufacturing when using molding or casting manufacturing techniques. Note that, apart from the performance of a structure, the manufacturing constraints or the geometric constraints are important, and some modifications are necessary. To test this feature, we compared the compliances of a straight design (20% mass constraint) in Fig. 17(*c*). Based on the compliances of Figs. 17(*b*) and 17(*c*), the topology optimization can determine a ten times better design.

Figure 18 shows several design examples with shadow filters. The results show that the manufacturing constraints were successfully imposed. When light is emitted downward, the parting direction on the upper side can be realized for the optimal layout of Fig. 18(*a*). Compared with the designs in Figs. 17(*b*) and 17(*c*), Fig. 18(*a*) shows the optimal layout, which is similar to the optimal layout with the shape optimization or the level-set approach. In terms of the objective function, the design in Fig. 17(*b*) obviously outperforms the design from the shadow filter and the shape optimization. But, some modifications are inevitable due to manufacturing constraints, which hurt the performance. The reverse parting direction is imposed in Fig. 18(*b*) by changing the direction of the light. To draw the parting direction at the center of the design domain, we consider the two light sources in Fig. 18(*c*) and the parting line at the center. The optimal layout in Fig. 18(*c*) can be regarded as an assembled structure of the upper and the bottom structures. Higher compliances can be obtained compared with the compliance in Fig. 17. Figure 19 shows some optimal layouts with different vertical locations of the parting lines with the conditions of Fig. 18(*c*). With the parting lines offset from the center, the optimal distributions exist only at the bottom domain or the upper domain except in the vertical line structures. Dramatic changes in optimal layout were observed for the parting lines between 22 and 27 of the vertical location. By imposing the manufacturing constraint, the local optimum issue becomes serious. Some nonoptimal features appear in Fig. 19. In addition, the initial design variable becomes important. In this example, the evenly distribution of the design variable is used.

Figure 20 shows the optimal designs with the heuristic shadow filters, which replace the design variables with the filtered design variables at every iteration. This approach is a heuristic approach, but we can obtain some optimized layouts.

Example 4: Conjugate Heat Transfer Problem. For the next example, the topology optimization for the conjugate heat transfer problem is carried out with the shadow filter. The objective function is to maximize the heat dissipation through the forced convection considering the manufacturing constraint. For this multiphysics problem, the coupled simulation of Navier–Stokes equation and heat transfer equation is conducted (see Sec. 2 and Ref. [15] for more details). While solving this topology optimization problem, the multiple local optima issue in Fig. 21 is observed; it is possible to obtain an identical shadow image with different design variables

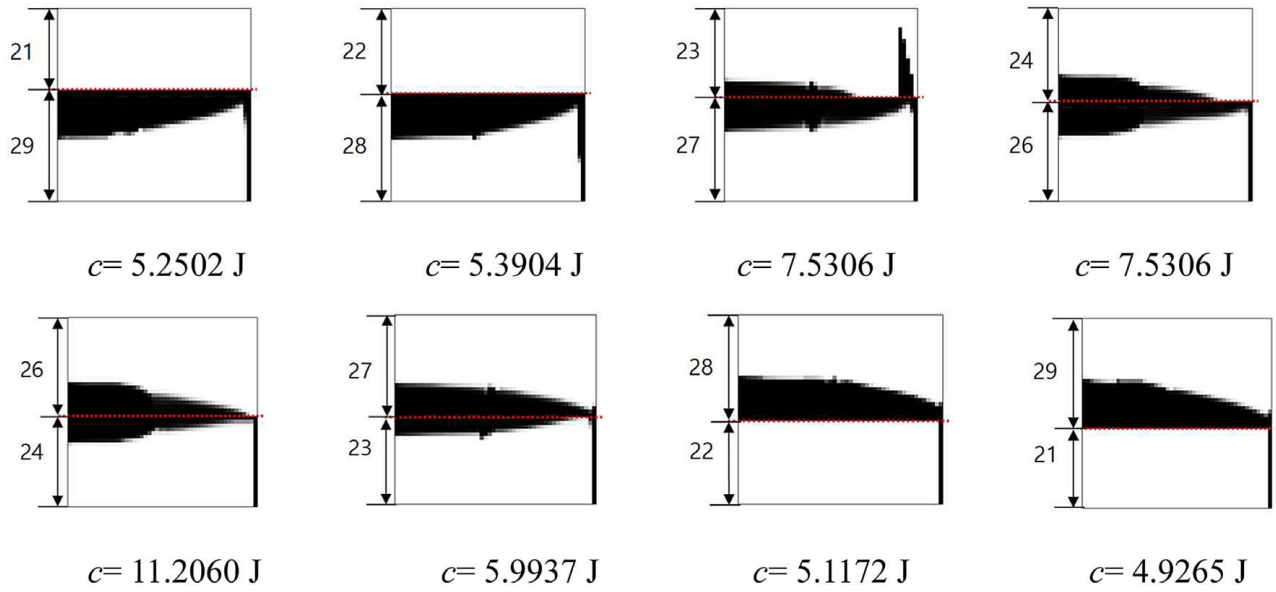

Fig. 19 Effect of the parting line

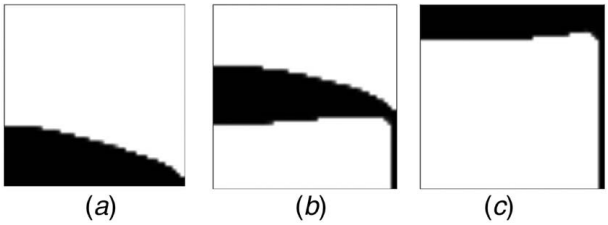

Fig. 20 Designs with the heuristic shadow filters: (*a*) $c = 2.5161$ J, (*b*) $c = 3.1191$ J, and (c) $c = 6.5352$ J

and it causes the convergence difficulty in this multiphsyics topology optimization. Thus, we resolve this issue by adding the sum of the design variables to the thermal compliance as (47)

$$\text{Min} \int_{q_{in}} T \times q_{in} d\Gamma - \theta \int_{\Omega_d} \gamma dv \, \theta\text{: scaling factor}$$

$$\text{Subject to } V(\tilde{\boldsymbol{\gamma}}) \leq \bar{\text{V}}$$

where design domain is denoted by Ω_d and the volume limit is denoted by $\bar{V}$. The scaling factor is θ. The mass constraint is set to 30% of the design domain. The optimum design without the geometric constraint (119.09 WK) is shown in Fig. 22(*b*). With the shadow filters, the optimum designs in Figs. 22(*c*)–22(*g*) can be obtained. By considering the manufacturing constraint, the objective values are increased slightly but it is successful to apply the manufacturing constraint for this multiphysics problem. The detail procedure of the shadow density filter for Fig. 22(*g*) is presented in Fig. 23.

Example 5: Fluid–Structure Interaction Problem. For the next example, the syntheses of the compliant mechanism layouts maximizing the output displacement at the location of the spring in Fig. 24 are considered using the shadow filter. The analysis domain consists of the three domains: the left fluid domain, the middle nondesign domain fixed as a flexible solid domain, and the right design domain. At the middle of the right most side, the pressure input condition is applied. Due to the middle nondesign domain, the direction of the input fluid flow is subject to be changed inside the left fluid domain. Consequently the middle nondesign domain would deflect toward the right direction due to the change of the momentum of the input fluid and the transmitted fluid force. Figure 24(*b*) shows the optimum design without the shadow filter. It is worthy to note that this design can be manufacturable in the horizontal direction. Therefore, this example can be tested to check the effect of the filter to the optimization condition and the local optima issue. To control the direction of the molding,

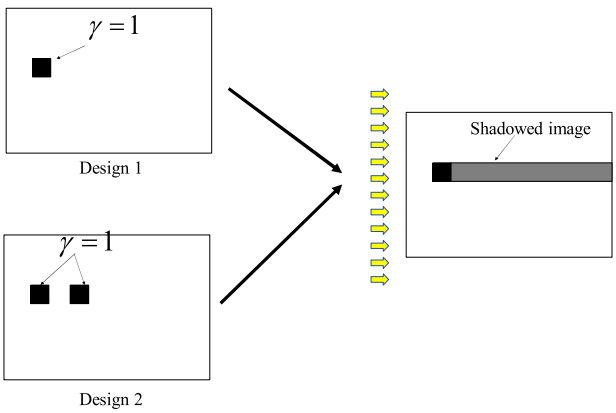

Fig. 21 An illustration of multiple local optima issue with the shadow density filter

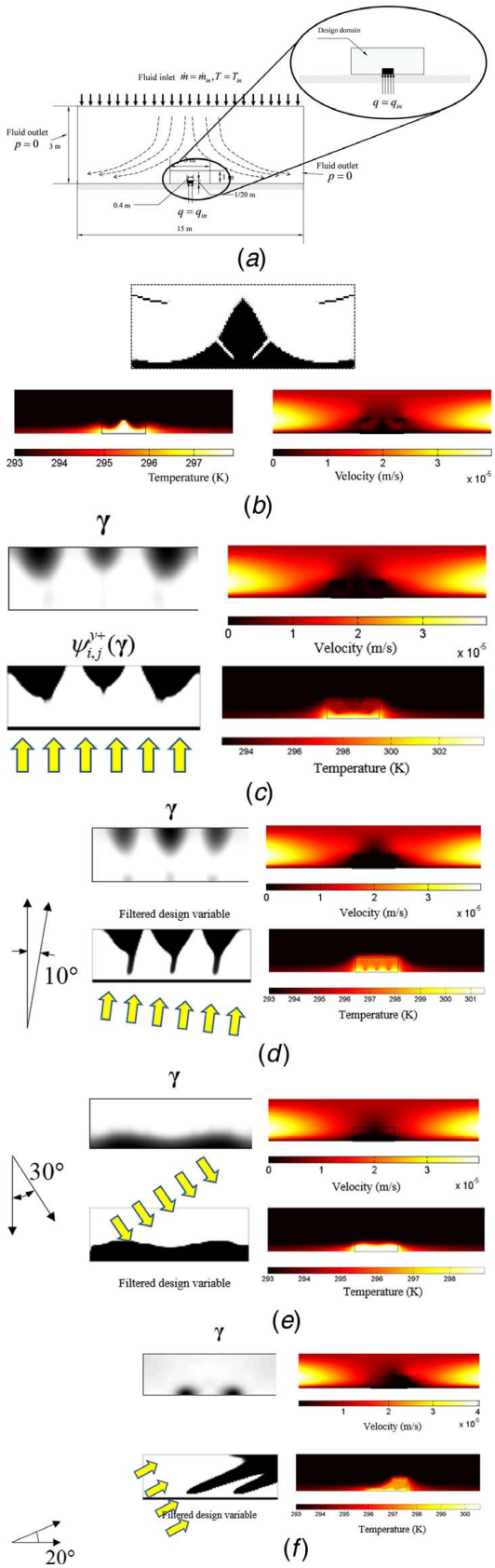

Fig. 22 The heat dissipation structure designs using the forced convection: (*a*) the problem definition (fluid: $\rho_{water} = 1000$ kg/m^3, $\eta_{water} = 1.308 \times 10^{-3}$ Pa · s, $k_{air} = 0.6$ W/m · K, $C_{water} = 4184$ J/kg · K, solid: $\rho_s = 8920$ kg/m^3, $C_s = 3.45 \times 10^6$ J/kg · K, $k_s = 401$ W/m · K, $\dot{m}_{in} = 0.0025$ kg/s, $T_{in} = 293$ K, $q_{in} = 100$ W/m^2) [15] and (*b*) the optimum design without the shadow filter (thermal compliance = 119.09 WK), (*c–f*) the optimum designs with the shadow filters.

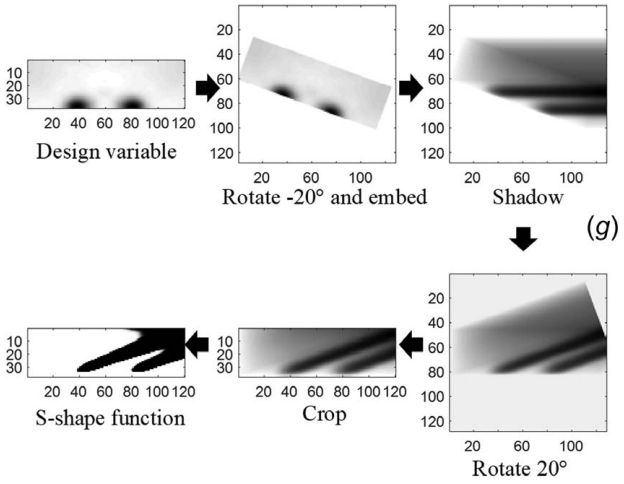

Fig. 23 The shadowing process for the result in Fig. 22(g)

the shadow density filter is applied for the results in Fig. 25. By changing the direction of the virtual light, it is possible to impose the molding constraint successfully. Due to the vertical structure, the pressure from the fluid part is not changed significantly. The purpose of this example is to show that the present shadow filter can be applied for this type of multiphysics system. By imposing the manufacturing constraint, the optimal structures maximizing the displacement at the working point can be obtained. The designs in in Fig. 25 are similar to the optimum layout of Fig. 24(*b*) with a lower objective value that implies that the present density filter at least can provide a similar local optimum maintaining the manufacturability

$$\text{Max } \Phi = u_s + \theta \int_{\Omega_d} \gamma dv \qquad (48)$$

$$\text{Subject to } V(\tilde{\boldsymbol{\gamma}}) \le \bar{V}$$

Example 6: Three-Dimensional Design Example. For the next example, the three-dimensional cantilever beam problem with a uniform load in Fig. 26 is considered with the application of the shadow density filter. The standard X-shaped beam appears

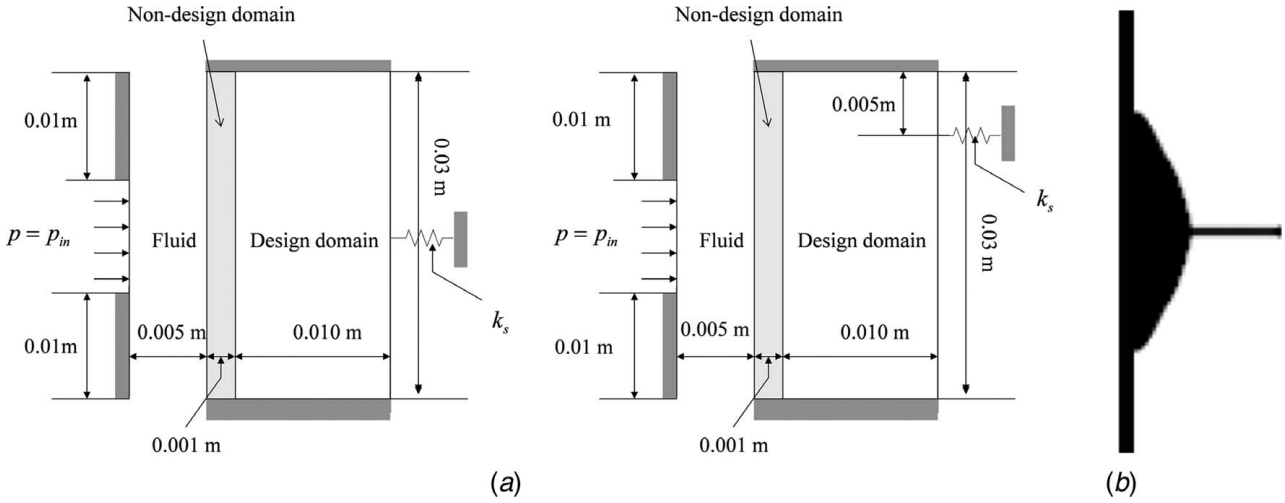

Fig. 24 (*a*) Problem definition of the compliant mechanisms and (*b*) an optimal layout without the shadow filter ($\rho = 1000$ kg/m^3, $\mu = 1.002$ mkg/ms, $C_s = 0.1$ MPa, $\nu = 0.3$, V^*: 30%, $\alpha_{max} = 10^{12}$, $p_{in} = 0.01$ N/m^2, $k_s = 100$ N/m)

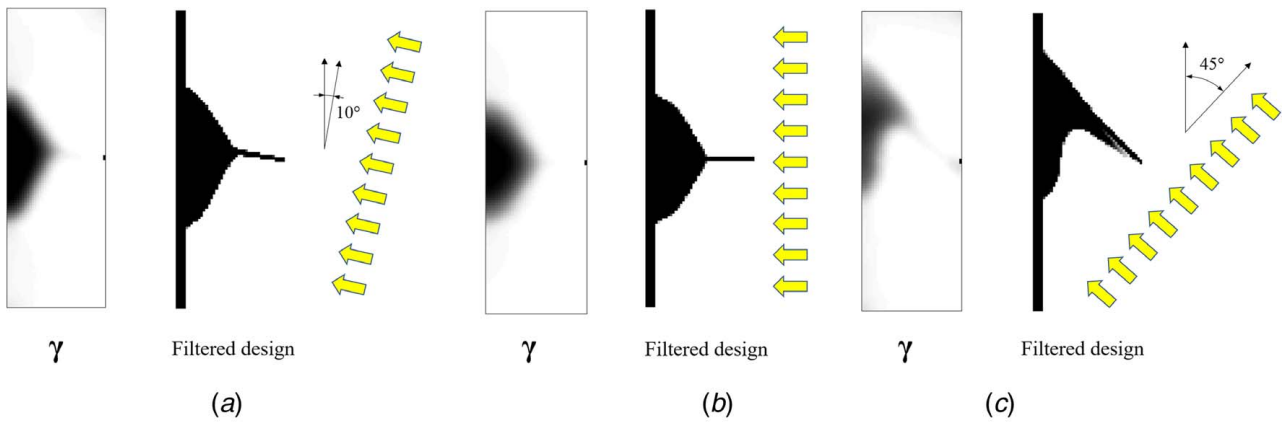

Fig. 25 Optimal designs with the shadow filter: (*a*) an optimum design with the horizontal virtual light (displacement = 7.2073×10^{-7} m), (*b*) an optimum design with the virtual light (10 deg) (displacement = 5.885×10^{-7} m), and (c) an optimum design with the virtual light (45 deg) (displacement = 5.3083×10^{-7} m)

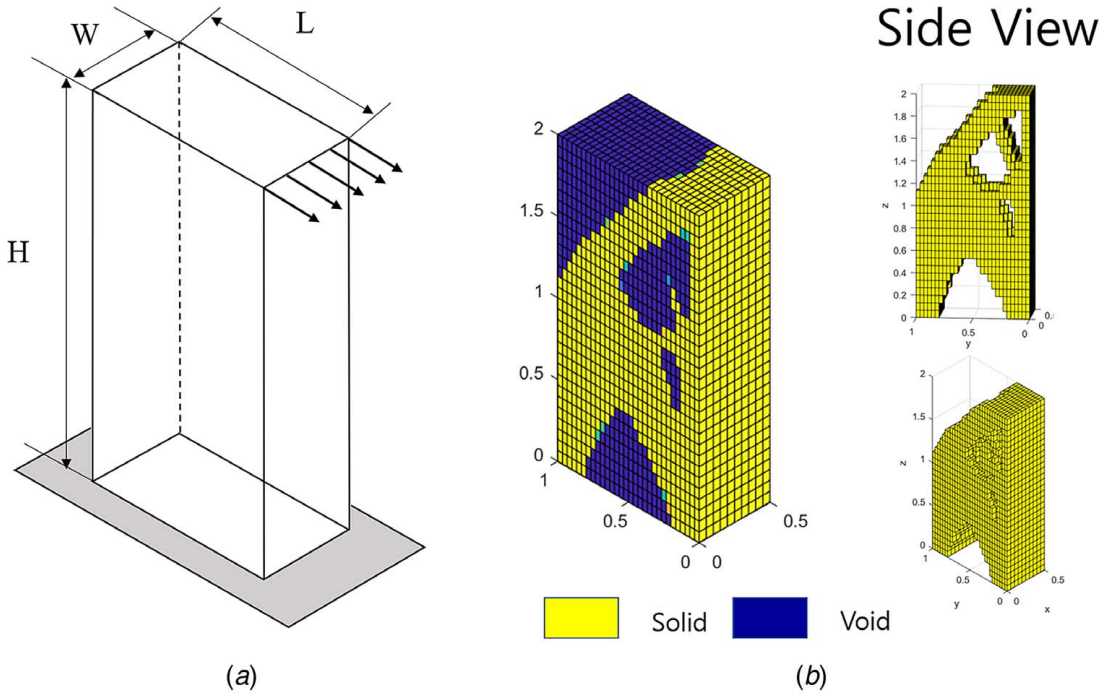

Fig. 26 A three-dimensional problem with the SIMP approach: (*a*) the problem definition and (*b*) optimal layout

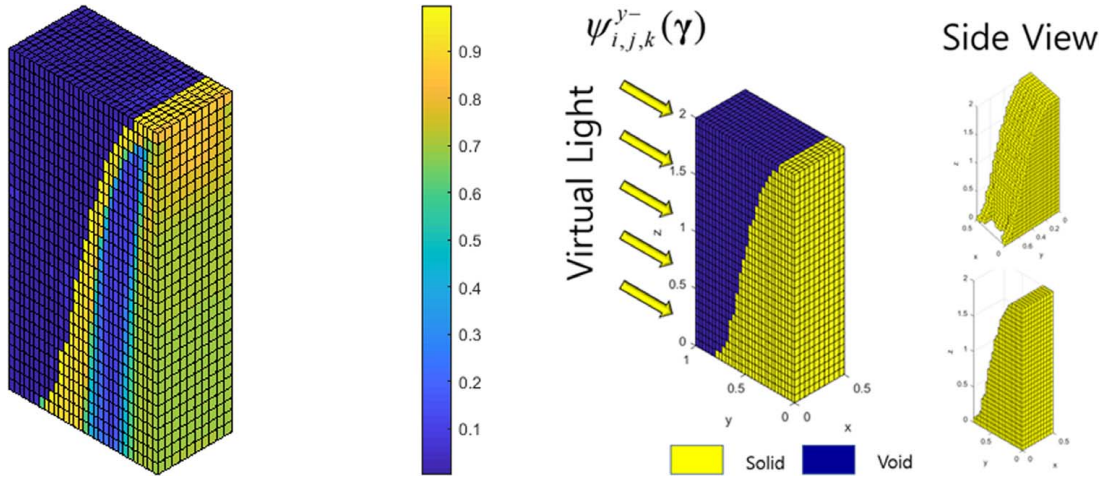

Fig. 27 Optimum design with $\psi^{y-}_{i,j,k}(\gamma)$

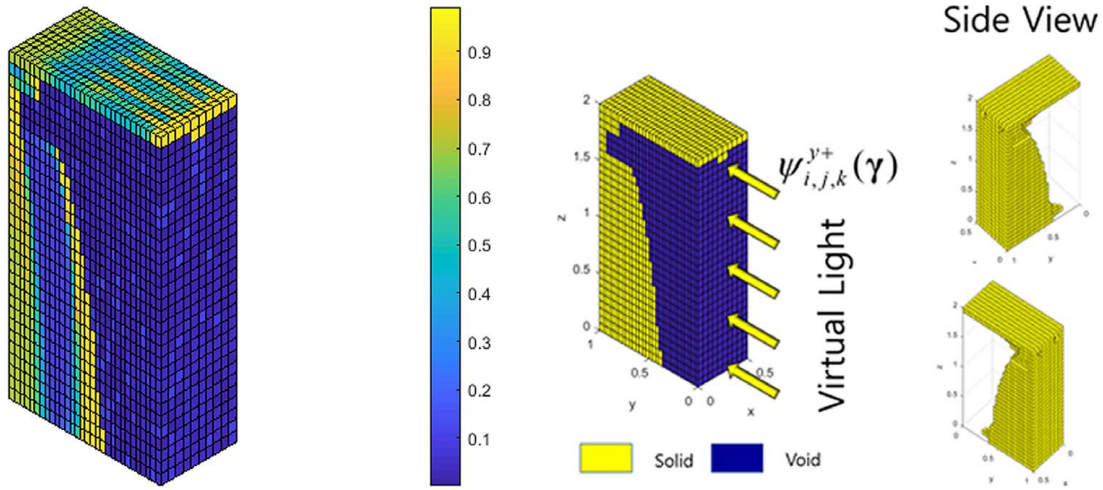

Fig. 28 Optimum design with $\psi^{y+}_{i,j,k}(\gamma)$

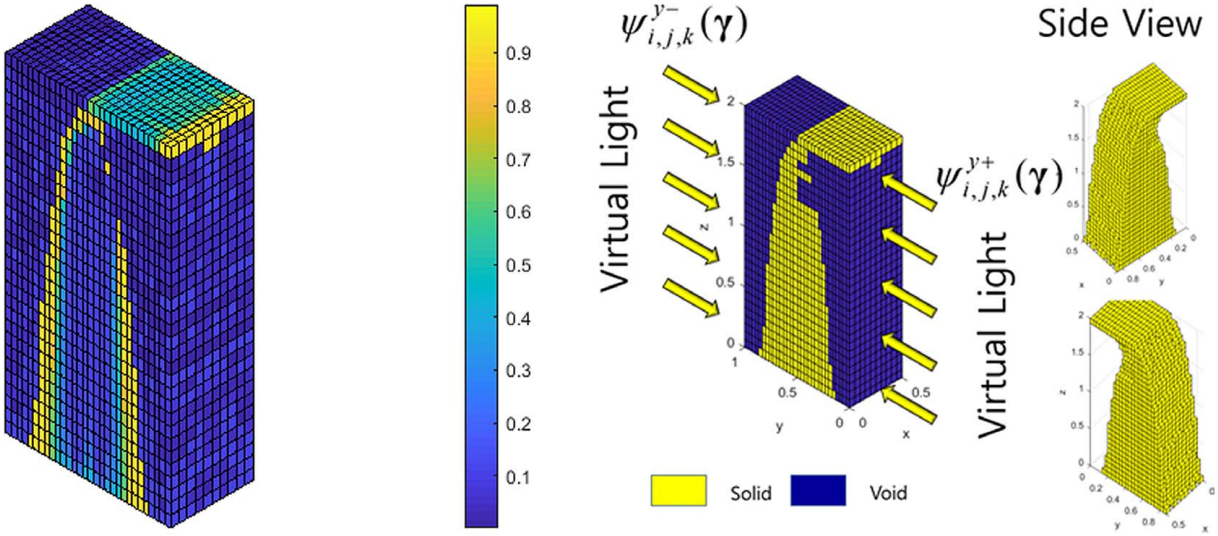

Fig. 29 Optimum design with $\psi^{y-}_{i,j,k}(\gamma) \times \psi^{y+}_{i,j,k}(\gamma)$

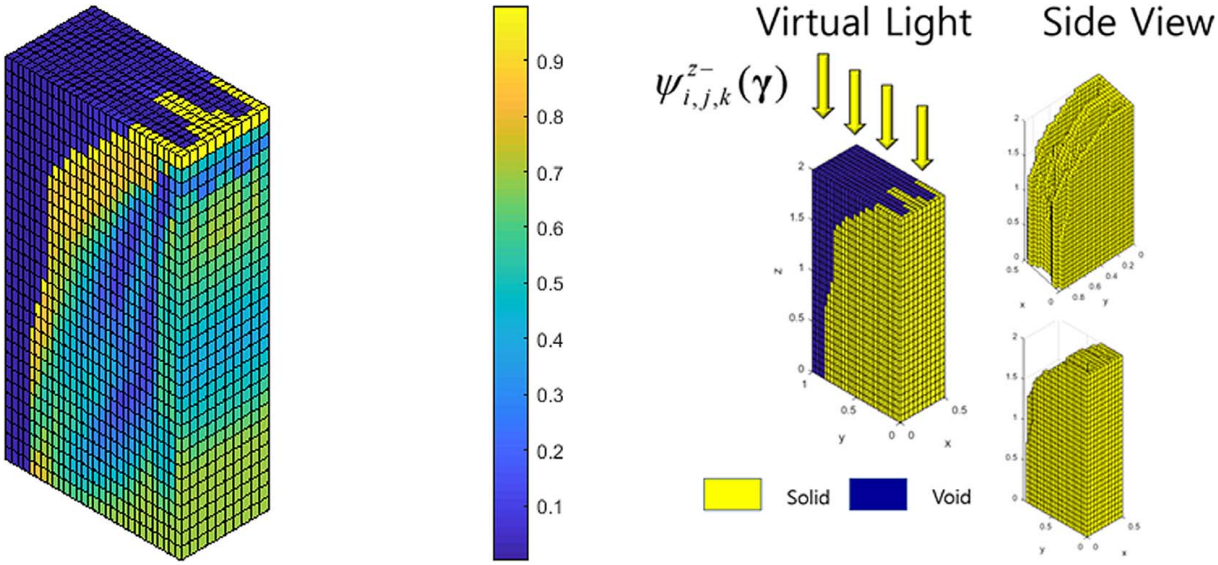

Fig. 30 Optimum design with $\psi^{z-}_{i,j,k}(\gamma)$

around the center, which makes it hard to manufacture using the casting manufacturing process. First, Fig. 27 shows the optimal layout with the $\psi^{y-}_{i,j,k}(\gamma)$ filter (note that now the filter is defined in three-dimensional space) or the light from the left side surface toward the right-side surface. The optimal shape manufacturable with the molding or the casting can be obtained here due to the imposed manufacturing condition. Figures 28 and 29 also show the optimal layouts with the different conditions. Figure 30 shows an optimal topology with $\psi^{z-}_{i,j,k}(\gamma)$. We found that all examples satisfy the manufacturing constraint using the shadow density filter. This example shows that the present shadow filter can be efficiently applied in three-dimensional problems too. As the shadow filter is composed with the multiplications of scalars, the computational effort can be neglected in comparison with the effort of the finite element simulation. For the three-dimensional problem, the time of the application of the shadow filter takes 0.0019 s when one finite element simulation takes 10.3928 s.

Conclusions

This research develops a new type of filter referred to as the shadow density filter, which mimics X-rays or shadows to directly impose some manufacturing constraints in the topology optimization problem. Manufacturing constraints are important in real applications but often have been neglected in the solutions of topology optimization. Recent interest in imposing the manufacturing constraints in topology optimization has increased. There are two common approaches for realizing this: adding some manufacturing constraints or density filtering. The present shadow density filter also achieves this purpose using a density filtering approach for manufacturing. Compared with approaches that solve temperature equations or light equations to impose the manufacturing constraints [1,2], the present approach considers the manufacturability issue without solving extra physics problem.

The implemented shadow filters have some design variables in a domain and they are shadowed in various directions due to the

combinations of lights. Then, the shadows of the design variables were projected by the *s*-shape function. The developed shadow filter is a combination of many local linear multiplications of the design variables. This is one of the benefits of this approach, and it shows some new features compared with the other approaches. To prove the validity of the method, several topology optimization problems (compliance minimization problem, heat dissipation structure design problem and mechanism design problem considering fluid–structure interaction) were solved. The designs obtained with the shadow filter suggest that the present approach enables us to efficiently obtain optimal layouts ready for manufacturing but only by sacrificing the performance. In addition, the present shadow filter can be applied for multiple materials. We expect that the present shadow filter can be applied for 3D printing manufacturing schemes. Moreover, the extension of manufacturing constraints for irregular meshes or shell elements should be conducted.

Conflict of Interest

There are no conflicts of interest.

Data Availability Statement

The datasets generated and supporting the findings of this article are obtainable from the corresponding author upon reasonable request. The authors attest that all data for this study are included in the paper.

References

[1] Li, Q., Chen, W., Liu, S., and Tong, L., 2016, "Structural Topology Optimization Considering Connectivity Constraint," Struct. Multidiscipl. Optim., **54**(4), pp. 971–984.

[2] Sato, Y., Yamada, T., Izui, K., and Nishiwaki, S., 2017, "Manufacturability Evaluation for Molded Parts Using Fictitious Physical Models, and its Application in Topology Optimization," Int. J. Adv. Manuf. Technol., **92**(1–4), pp. 1391–1409.

[3] Gersborg, A. R., and Andreasen, C. S., 2011, "An Explicit Parameterization for Casting Constraints in Gradient Driven Topology Optimization," Struct. Multidiscipl. Optim., **44**(6), pp. 875–881.

[4] Berrocal, L., Fernández, R., González, S., Periñán, A., Tudela, S., Vilanova, J., Rubio, L., Martín Márquez, J. M., Guerrero, J., and Lasagni, F., 2019, "Topology Optimization and Additive Manufacturing for Aerospace Components," Prog. Addit. Manuf., **4**(2), pp. 83–95.

[5] Boothroyd, G., Dewhurst, P., and Knight, W. A., 2001, *Product Design for Manufacture and Assembly, Revised and Expanded*, CRC Press, Boca Raton, FL.

[6] Hoque, A., Halder, P., Parvez, M., Szecsi, T. J. C., and Engineering, I., 2013, "Integrated Manufacturing Features and Design-for-Manufacture Guidelines for Reducing Product Cost Under CAD/CAM Environment," Comput. Ind. Eng., **66**(4), pp. 988–1003.

[7] James, B. D., Spisak, A. B., and Colella, W. G., 2014, "Design for Manufacturing and Assembly Cost Estimate Methodology for Transportation Fuel Cell Systems," ASME J. Manuf. Sci. Eng., **136**(2), p. 024503.

[8] Selvaraj, P., Radhakrishnan, P., and Adithan, M., 2009, "An Integrated Approach to Design for Manufacturing and Assembly Based on Reduction of Product Development Time and Cost," Int. J. Adv. Manuf. Technol., **42**(1–2), pp. 13–29.

[9] Salonitis, K., 2016, "Design for Additive Manufacturing Based on the Axiomatic Design Method," Int. J. Adv. Manuf. Technol., **87**(1–4), pp. 989–996.

[10] Zhou, M., Fleury, R., Shyy, Y.-K., Thomas, H., and Brennan, J., "Progress in Topology Optimization with Manufacturing Constraints," Proc. 9th AIAA/ISSMO Symposium on Multidisciplinary Analysis and Optimization, p. 5614.

[11] Zhou, M. D., Lazarov, B. S., Wang, F. W., and Sigmund, O., 2015, "Minimum Length Scale in Topology Optimization by Geometric Constraints," Comput. Methods Appl. Mech. Eng., **293**, pp. 266–282.

[12] Liu, J., and Ma, Y., 2016, "A Survey of Manufacturing Oriented Topology Optimization Methods," Adv. Eng. Softw., **100**, pp. 161–175.

[13] Langelaar, M., 2019, "Topology Optimization for Multi-Axis Machining," Comput. Methods Appl. Mech. Eng., **351**, pp. 226–252.

[14] Vatanabe, S. L., Lippi, T. N., Lima, C. R. d., Paulino, G. H., and Silva, E. C. N., 2016, "Topology Optimization with Manufacturing Constraints: A Unified Projection-Based Approach," Adv. Eng. Softw., **100**, pp. 97–112.

[15] Yoon, G. H., 2010, "Topological Design of Heat Dissipating Structure With Forced Convective Heat Transfer," J. Mech. Sci. Technol., **24**(6), pp. 1225–1233.

[16] Otomori, M., Yamada, T., Izui, K., Nishiwaki, S., and Andkjær, J., 2012, "A Topology Optimization Method Based on the Level set Method for the Design of Negative Permeability Dielectric Metamaterials," Comput. Methods Appl. Mech. Eng., **237–240**, pp. 192–211.

[17] Yoon, G. H., 2012, "Topological Layout Design of Electro-Fluid-Thermal-Compliant Actuator," Comput. Methods Appl. Mech. Eng., **209–211**, pp. 28–44.

[18] Noguchi, Y., Yamada, T., Otomori, M., Izui, K., and Nishiwaki, S., 2015, "An Acoustic Metasurface Design for Wave Motion Conversion of Longitudinal Waves to Transverse Waves Using Topology Optimization," Appl. Phys. Lett., **107**(22), p. 221909.

[19] Zhang, W., Li, D., Zhou, J., Du, Z., Li, B., and Guo, X., 2018, "A Moving Morphable Void (MMV)-Based Explicit Approach for Topology Optimization Considering Stress Constraints," Comput. Methods Appl. Mech. Eng., **334**, pp. 381–413.

[20] Zhang, W., Liu, Y., Du, Z., Zhu, Y., and Guo, X., 2018, "A Moving Morphable Component Based Topology Optimization Approach for Rib-Stiffened Structures Considering Buckling Constraints," ASME J. Mech. Des., **140**(11), p. 111404.

[21] Kim, Y. Y., and Yoon, G. H., 2000, "Multi-resolution Multi-Scale Topology Optimization—a new Paradigm," Int. J. Solids Struct., **37**(39), pp. 5529–5559.

[22] Yoon, G. H., and Kim, Y. Y., 2003, "The Role of S-Shape Mapping Functions in the SIMP Approach for Topology Optimization," KSME Int. J., **17**(10), pp. 1496–1506.

[23] Guest, J. K., and Zhu, M., "Casting and Milling Restrictions in Topology Optimization via Projection-Based Algorithms," Proc. ASME 2012 International Design Engineering Technical Conferences and Computers and Information in Engineering Conference, pp. 913–920.

[24] Yoon, G., Kim, Y., Bendsoe, M., and Sigmund, O., 2004, "Hinge-free Topology Optimization with Embedded Translation-Invariant Differentiable Wavelet Shrinkage," Struct. Multidiscipl. Optim., **27**(3), pp. 139–150.

[25] Allaire, G., Jouve, F., and Michailidis, G., 2016, "Thickness Control in Structural Optimization via a Level Set Method," Struct. Multidiscipl. Optim., **53**(6), pp. 1349–1382.

[26] Langelaar, M., 2016, "Topology Optimization of 3D Self-Supporting Structures for Additive Manufacturing," Addit. Manuf., **12**, pp. 60–70.

[27] Gaynor, A. T., and Guest, J. K., 2016, "Topology Optimization Considering Overhang Constraints: Eliminating Sacrificial Support Material in Additive Manufacturing Through Design," Struct. Multidiscipl. Optim., **54**(5), pp. 1157–1172.

[28] Brackett, D., Ashcroft, I., and Hague, R., "Topology Optimization for Additive Manufacturing," Proc. Proceedings of the Solid Freeform Fabrication Symposium, Austin, TX, pp. 348–362.

[29] Xia, Q., Shi, T. L., Wang, M. Y., and Liu, S. Y., 2010, "A Level set Based Method for the Optimization of Cast Part," Struct. Multidiscipl. Optim., **41**(5), pp. 735–747.

[30] Qian, X. P., 2017, "Undercut and Overhang Angle Control in Topology Optimization: A Density Gradient Based Integral Approach," Int. J. Numer. Meth. Eng., **111**(3), pp. 247–272.

[31] Allaire, G., Jouve, F., and Michailidis, G., 2016, "Molding Direction Constraints in Structural Optimization Via a Level-Set Method," *Variational Analysis and Aerospace Engineering*, A. Frediani, B. Mohammadi, O. Pironneau, and V. Cipolla, eds., Springer, New York, pp. 1–39.

[32] Guest, J. K., Prevost, J. H., and Belytschko, T., 2004, "Achieving Minimum Length Scale in Topology Optimization Using Nodal Design Variables and Projection Functions," Int. J. Numer. Meth. Eng., **61**(2), pp. 238–254.

[33] Dienemann, R., Schumacher, A., and Fiebig, S., "Topology Optimization Considering the Requirements of Deep-Drawn Sheet Metals," Proc. Proceedings of the 11th World Congress on Structural and Multidisciplinary Optimization, Sydney, Australia.

[34] Chen, S., Wang, M. Y., and Liu, A. Q., 2008, "Shape Feature Control in Structural Topology Optimization," Comput.-Aided Des., **40**(9), pp. 951–962.

[35] Yoon, G. H., 2010, "Topology Optimization for Stationary Fluid-Structure Interaction Problems Using a new Monolithic Formulation," Int. J. Numer. Meth. Eng., **82**(5), pp. 591–616.

[36] Joshi, D., and Ravi, B., 2010, "Early Castability Evaluation Using Analytical Hierarchy Process," Int. J. Adv. Manuf. Technol., **50**(1–4), pp. 21–36.

[37] Armillotta, A., Fasoli, S., and Guarinoni, A., 2016, "Cold Flow Defects in Zinc die Casting: Prevention Criteria Using Simulation and Experimental Investigations," Int. J. Adv. Manuf. Technol., **85**(1–4), pp. 605–622.

[38] Liu, S.-G., Jin, Q., Wang, P., and Xie, R.-J., 2014, "Closed-form Solutions for Multi-Objective Tolerance Optimization," Int. J. Adv. Manuf. Technol., **70**(9–12), pp. 1859–1866.